On Tone-Burst Measurements of Sound Speed and Attenuation in Sandy Marine Sediments

Michael J. Buckingham and Michael D. Richardson

***Abstract*—During the Sediment Acoustics Experiment in 1999 (SAX99), the *in Situ* Sediment geoAcoustic Measurement System (ISSAMS), transmitting tone bursts containing an integer number of cycles, was used to measure the speed and attenuation of compressional waves in a weakly dispersive, medium-sand sediment in the Gulf of Mexico. ISSAMS was deployed at seven stations and operated mostly at a frequency of 38 kHz, but at two of the sites, a succession of pulses was transmitted with frequencies extending from 25 to 100 kHz, in 5-kHz increments, yielding the phase speed, the group speed and the attenuation as a function of frequency. An analysis of a tone-burst transmission in a dispersive medium illustrates that several subtle factors, including the narrow bandwidth of the source, along with dispersion and attenuation in the medium, have the potential for introducing significant errors into travel-time measurements. It is concluded that, in general, the timing is best performed between two receivers rather than between the source and a receiver, the difficulty in the latter case being that the output from a narrow-band source is not a replica of the input. A correlation applied to the arrivals at the two receivers yields the travel time, from which a good approximation to the group speed is immediately available. Alternatively, a Fourier decomposition yields the phase speed as a function of frequency, which would be an advantage in a highly dispersive medium. The two techniques return almost identical wave speeds when applied to the ISSAMS tone-burst data from the weakly dispersive SAX99 sediments: at 38 kHz, the mean wave speed from the six primary stations is 1778 m/s. Attenuation was also estimated from receiver-to-receiver travel paths, using three different techniques: the ratio of the mean-square values of the arrivals, the ratio of the Fourier magnitudes of the arrivals and transposition. All three methods yield similar results when applied to the SAX99 data, returning a mean attenuation from the six stations of 12 dB/m at 38 kHz, which is comparable with previously reported measurements of attenuation in marine sands. From the broadband measurements, between 25 and 100 kHz, the dispersion is found to be weak but detectable and the attenuation scales almost linearly with frequency, which corresponds to a nearly constant Q.**

***Index Terms*—Acoustic signal measurement, acoustic velocity measurement, attenuation measurement, sea floor, sediments.**

Manuscript received December 21, 2001; revised April 13, 2002. The work of M. J. Buckingham was supported by the Office of Naval Research, Ocean Acoustics Code (Dr. Jeffrey Simmen) under Grant N00014-93-1-0054. The work of M. D. Richardson was supported in part by Work Request N00014-02-WX20256 and in part by the Naval Research Laboratory Program Element N0601153N.

M. J. Buckingham is with the Marine Physical Laboratory, Scripps Institution of Oceanography, University of California, San Diego, La Jolla, CA 92093-0238 USA. He is also with the Institute of Sound and Vibration Research, The University, Southampton SO17 1BJ, U.K.

M. D. Richardson is with the Marine Geosciences Division, Naval Research Laboratory, Stennis Space Center, MS 39529 USA.

Publisher Item Identifier S 0364-9059(02)06414-2.

I. Introduction

SEDIMENT ACOUSTICS Experiment 1999 (SAX99) [1], [2] is part of a research initiative, sponsored by the Office of Naval Research (ONR), on the interaction of high-frequency sound with marine sediments. The multidisciplinary experiment was performed from late September to mid November 1999, in the northeastern Gulf of Mexico, 2-km off Fort Walton Beach, FL, at a site where the water is 18–19 m deep. At this location, the sea bed consists of a well-sorted medium sand with a mean grain diameter of 420 μm (1.25 ϕ units) and a mean sorting of 0.63 ϕ units [1]. The porosity of the sediment was determined using three different laboratory techniques: gravimetric analysis of diver-collected cores [3], and two *in situ* methods involving electrical conductivity probes [4], [5]. The fractional porosity of the SAX99 sands was found to be $N \approx 0.38$, with a spread of 8% between the 95% confidence limits. This result is consistent with many measurements of the porosity of marine sands that have been reported in the literature, as summarized by Buckingham [6]. It suggests that the packing of the grains in a medium or coarser sand can be modeled as a random packing of smooth spheres, a structure which is known to show a porosity very close to 0.38 [7].

As part of SAX99, the remotely operated *In Situ* Sediment geoAcoustic Measurement System (ISSAMS) [8], [9] was deployed to measure the speed and attenuation of both compressional and shear waves, along with the electrical resistivity and shear strength of the sediment. In this paper, we concern ourselves only with the compressional wave speed and attenuation. ISSAMS typically uses four fixed, mounted, compressional-wave probes, which are hydraulically driven into the sediment to precise depths [10]. The probes are of two types, either identical, radially poled ceramic cylinders or nearly identical 1–3 poled rectangular, solid piezo-ceramics. Both types of probe can be used as either an acoustic source or receiver. Representative source–receiver configurations are illustrated in Fig. 3 of Barbagelata *et al.* [8]. With this system, the compressional wave speed and attenuation can be measured over source–receiver path lengths ranging between 10 and 130 cm, and down to depths of 30 cm beneath the seawater-sediment interface.

In most of the SAX99 deployments, a tone burst consisting of a 6-cycle, 38-kHz sine wave was used as the voltage input to the source. Initially, the sediment sound speed was calculated from time-of-flight *differences* between water and sediment (cross-correlation of the two received waveforms) and values of attenuation were evaluated from ratios of received voltage between

the four transducers, using the transposition technique described by Richardson [10]. Both, wave speed and attenuation measurements, require a precision estimate of the source-to-receiver distance, which was obtained from a seawater calibration: the acoustic travel time was measured in the water column immediately above the sea floor, where the sound speed was known from CTD casts, thus allowing the transducer separation to be evaluated.

A preliminary analysis of the compressional wave data from the SAX99 site yielded a mean sound speed of 1739 m/s and a mean attenuation of 12.7 dB/m [1]. However, the greater source-to-receiver separations showed a trend toward higher estimated sound speeds [shown later in Fig. 15(a)]. This nonphysical observation triggered the collection of more data, from 10 additional deployments of ISSAMS, with transducer separations ranging between 10 and 130 cm. The resultant set of 40 compressional-wave speeds was similar to the earlier estimates in that the longer ranges yielded faster sound speeds.

In this article, the tone-burst technique for obtaining travel-time in a dispersive medium, such as a marine sediment, is examined theoretically. The range-dependence exhibited by the 38 kHz sound-speed estimates from ISSAMS deployments during SAX99 is found to be an artifact of the narrow-band source. To eliminate such source effects, alternative travel-time methodologies are proposed, which utilize receiver-to-receiver rather than source-to-receiver paths. The inter-receiver technique yields a reliable estimate of the sound speed, which is independent of the range, as illustrated using the ISSAMS data from SAX99. Several inter-receiver methods for measuring the compressional wave attenuation are also discussed, all of which yield very similar estimates. At 38 kHz, these methods return values of the attenuation in the SAX99 sediment that are consistent with previous measurements of attenuation in marine sands, as reported by Hamilton [11], [12] and Richardson [13].

In addition to the measurements at 38 kHz, the sound speed and attenuation were measured, using 6-cycle, tone-burst, inter-receiver techniques, over the frequency band between 25 and 100 kHz. For these broad-band measurements, 1–3 poled piezoceramics were used as sources and receivers. The dispersion is found to be weak but observable and the attenuation scales nearly linearly with frequency.

II. Band-Limited Source

In ISSAMS, the standard compressional-wave transducers, used as both sources and receivers, are radially poled, cylindrical, piezoelectric tubes with OD $= 25$ mm, ID $= 21.8$ mm, and length 25 mm. Further details of the transducer design and performance specifications can be found in Barbagelata *et al.* [8]. At the frequencies of interest, source-shape effects on the radiated field are negligible and the square cross-section transducer may be satisfactorily modeled as a sphere of radius $b = 12.5$ mm.

Ideally, when the transducer is used as a source, a voltage waveform, $v(t)$, applied at the input terminals would produce an output in the form of a radial velocity pulse, $s_b(t)$, identical in shape to $v(t)$. In practice, however, this does not happen. Because of its mechanical resonance and the loading of the medium, the transducer has a limited pass band, the effects of which may be represented by a transfer function $H(j\omega)$, where ω is angular frequency and $j = \sqrt{-1}$. Since it is convenient to keep $H(j\omega)$ dimensionless, the source input voltage is taken to be normalized by a scaling factor of unity with dimensions of voltage/velocity, and thus the input as well as the output is treated as a velocity pulse. The output is the radial velocity, $s_b(t)$, of the (notionally) spherical source, which is related to the input "velocity," $s_{in}(t)$, by a product in the frequency domain

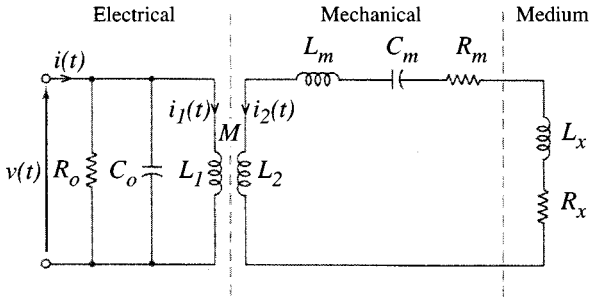

Fig. 1. Equivalent electrical circuit of the piezoelectric source transducer.

$$S_b(j\omega) = H(j\omega)S_{in}(j\omega) \tag{1}$$

where the uppercase symbols denote temporal Fourier transforms of their lowercase counterparts. As expressed in (1), the transfer function, H, between the input and output is indeed dimensionless.

An equivalent electrical circuit for the source transducer [14] is shown in Fig. 1. It consists of a transformer with mutual inductance M, representing the electro-mechanical coupling between the input and output circuits. Across the input terminals, a resistor R_o, and capacitor C_o, appear in parallel, representing, respectively, electrical losses and the clamped capacitance of the transducer. On the output side, the mechanical resonance of the transducer is represented by a series combination of an inductor L_m, a capacitor C_m and a resistor R_m. The loading of the medium is represented by an inductor L_x, and a resistorR_x, in series with the mechanical components. Obviously, the combined effect of the mechanical resonance and the loading of the medium is represented by a series L–C–R circuit in which the inductance is $L = L_m + L_x$, the capacitance is $C = C_m$, and the resistance is $R = R_m + R_x$.

The analog of radial velocity in the output circuit is current or, equivalently, voltage across the resistor, R. An elementary argument, which is developed in the Appendix, leads to a simple relationship between the output voltage across R and the input voltage, $v(t)$. In the frequency domain, the ratio of these two voltages is just the source transfer function H in (1), which can be expressed in the form

$$H(j\omega) = \frac{H_o}{1 + jQ\left(\frac{\omega}{\omega_o} - \frac{\omega_o}{\omega}\right)} \tag{2}$$

where H_o is a real, frequency-independent scaling factor (gain), and ω_o and Q are, respectively, the resonance angular

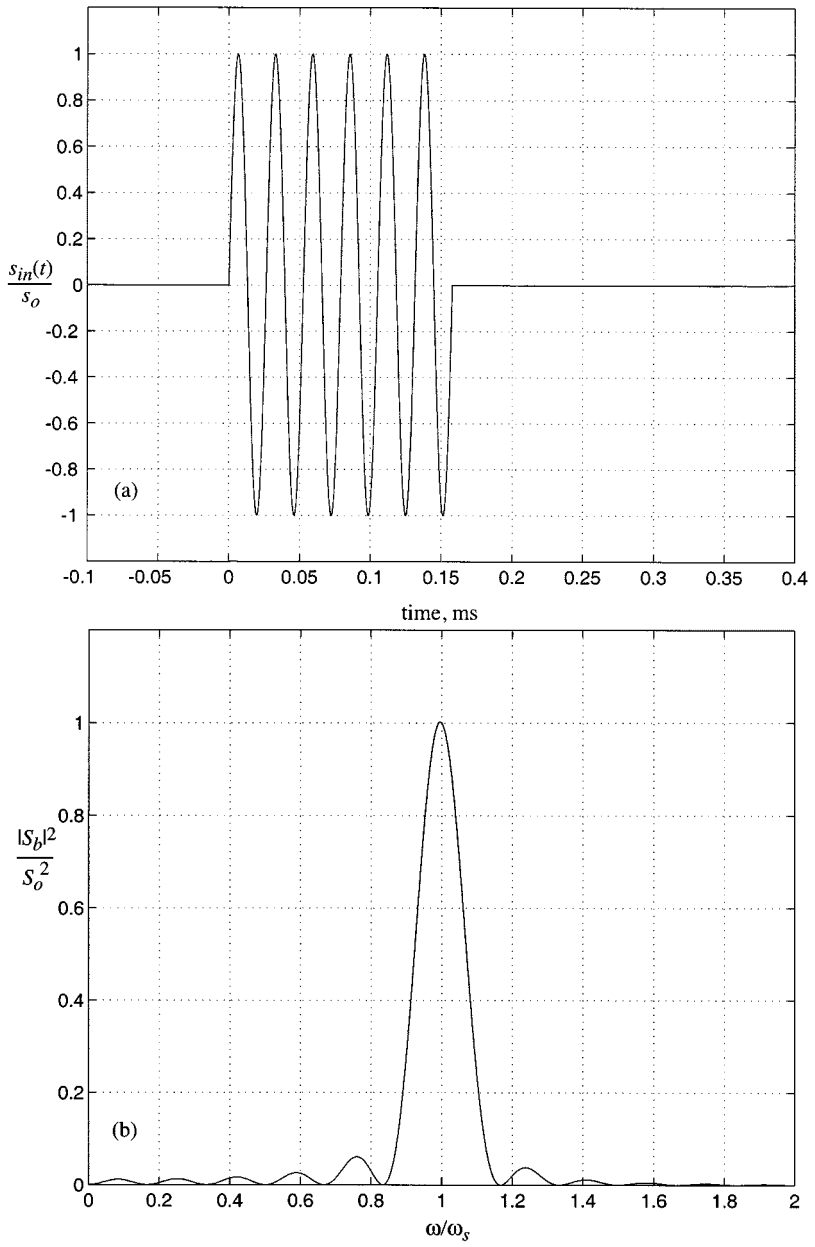

Fig. 2. (a) Sinusoidal input pulse from (5). (b) Its power spectrum from (7) ($m = 6$ and $\omega_s/2\pi = 38$ kHz).

frequency and the quality factor of the output circuit of the transducer

$$\omega_o = \frac{1}{\sqrt{LC}} \tag{3}$$

and

$$Q = \frac{1}{R}\sqrt{\frac{L}{C}} = \frac{1}{\omega_o RC} = \frac{\omega_o L}{R}. \tag{4}$$

Since L and R include the additive effects of the loading by the surrounding medium, the resonance properties of the source may be expected to differ slightly in sand and water. (*N.B.* An ideal source transducer would have $Q = 0$, representing a flat, infinitely wide pass band, which produces no distortion between input and output, but this situation is not found in practice.)

III. Source Input and Output Pulses

During SAX99, the input waveforms applied to the ISSAMS source transducer were mainly sinusoidal tone-bursts of an integer number of cycles, as represented by the expression

$$s_{in}(t) = s_o[u(t) - u(t - \tau_m)]\sin\omega_s t \tag{5}$$

where s_o is the amplitude of the input "velocity," ω_s is the angular frequency of the truncated sinusoid, t is time and $u(\cdots)$ is the Heaviside unit step function. The duration of the pulse in (5) is

$$\tau_m = \frac{2\pi m}{\omega_s} \tag{6}$$

where m is an integer representing the number of cycles in the input waveform. Fig. 2(a) shows an example of a 6-cycle,

38 kHz sinusoidal pulse, as computed from (5). [*N.B.* In the SAX99 experiments, a signal generator with very low internal impedance was used to drive the source and thus the effect of loading by the source was negligible. As confirmed by continuous monitoring, the input pulses showed no distortion but had exactly the form represented by (5) and illustrated in Fig. 2(a)].

The temporal Fourier transform of the input "velocity" pulse in (5) is

$$S_{in}(j\omega) = \frac{s_o \omega_s}{(\omega^2 - \omega_s^2)} \left(e^{-j\omega\tau_m} - 1\right). \tag{7}$$

The square of the magnitude of this function, normalized to $S_o^2 = (s_o m\pi/\omega_s)^2$, is plotted in Fig. 2(b) against dimensionless frequency, ω/ω_s. At the half-power points, the half-width of the principal maximum in the spectrum is approximately 0.43 ω_s/m, indicating that the 38-kHz, six cycle pulse shown in Fig. 2(a) contains significant spectral components over the frequency band from 36.4 to 39.6 kHz. The Fourier transform of the output velocity pulse is, from (1) and (2)

$$S_b(j\omega) = s_o\omega_s \frac{\left(e^{-j\omega\tau_m} - 1\right)}{(\omega^2 - \omega_s^2)} H_o \left[1 + jQ\left(\frac{\omega}{\omega_o} - \frac{\omega_o}{\omega}\right)\right]^{-1} \tag{8}$$

from which it is evident that, for realistic values of Q, the source velocity is not a facsimile of the input sinusoidal pulse.

The oscillating source generates a spherically symmetric pressure wave in the surrounding medium. In general, the medium will be dissipative, in which case the pressure pulse will exhibit attenuation and frequency dispersion, both of which can be represented through a complex sound speed, c. A straightforward derivation for the field from a spherical source yields the Fourier transform of the radiated pressure pulse as

$$P(j\omega) = \frac{j\omega\rho c_o^2 b^2 S_b}{c^2 r} \left(1 + j\,\frac{\omega}{c}\,b\right)^{-1} \exp\left[-j\,\frac{\omega}{c}\,(r-b)\right], \quad r \geq b \tag{9}$$

where r is the radial distance from the center of the source, ρ is the bulk density of the medium, and the real quantity c_o is the speed of sound in the material in the limit of low frequency.

By taking the inverse Fourier transform of (9), the pressure pulse transmitted into the medium may be expressed as

$$p(t, r) = \frac{j\rho c_o^2 b^2}{2\pi r} \int_{-\infty}^{\infty} \frac{\omega S_b}{c^2} \left(1 + j\,\frac{\omega b}{c}\right)^{-1} \cdot \exp\left[j\omega\left\{t - \frac{(r-b)}{c}\right\}\right] d\omega. \tag{10}$$

Since the receiver hydrophones respond to the acoustic pressure, (10) and (8) together provide a useful tool for investigating the characteristics of the pulse arrivals in the SAX99 travel-time and attenuation measurements.

IV. Water Column Pulses

Before making measurements in the sediment, the source-to-receiver and receiver-to-receiver ranges in ISSAMS were acoustically calibrated from tone-burst transmissions in the water column, where the sound speed, c_w, was known from CTD casts (see Richardson *et al.* [1, Fig. 7]). Before discussing the calibration procedure, it is useful to examine the shape of the pulses in the water column.

A. Theoretical Pulse Shapes

Since dispersion and attenuation are negligible in seawater for the ranges and frequencies of interest, c_w is real and independent of frequency. In this case, the expression for the pressure pulse in (10) takes the following form:

$$p(t, r) = \frac{j\rho_w b^2}{2\pi r} \int_{-\infty}^{\infty} \omega S_b \left(1 + j\,\frac{\omega b}{c_w}\right)^{-1} \cdot \exp\left[j\omega\left\{t - \frac{(r-b)}{c_w}\right\}\right] d\omega \tag{11}$$

where ρ_w is the density of seawater. The integral in (11) may be evaluated explicitly using contour integration. The integrand contains five simple poles and no other singularities. Symmetrically placed in the first and second quadrants are two poles, ω_1 and ω_2, from the transfer function, H, which is present in $S_b(j\omega)$

$$\omega_{1,2} = \pm\omega_{ow}\sqrt{1 - \frac{1}{4Q_w^2}} + \frac{j\omega_{ow}}{2Q_w} \tag{12}$$

where ω_{ow} and Q_w are, respectively, the resonance angular frequency and the Q of the source transducer when operating in seawater. A third pole, ω_3, associated with the finite size of the source, falls on the positive imaginary axis

$$\omega_3 = \frac{jc_w}{b}. \tag{13}$$

Two more poles, $\pm\omega_s$, symmetrically placed in the first and second quadrants and falling infinitesimally above the real axis, are found in the Fourier transform, (7), of the input velocity pulse, $S_{in}(j\omega)$.

By integrating around the top half-plane and performing a little algebra the following retarded-potential solution is obtained for the pressure pulse in the water column

$$p(t, r) = -p_o\,\frac{b}{r}\,\{u(t-\tau)F(t-\tau) - u(t-\tau-\tau_{\rm m})F(t-\tau-\tau_{\rm m})\} \tag{14}$$

where

$$p_o = \frac{\rho_w H_o s_o \omega_{ow} c_w}{Q\omega_s} \tag{15}$$

and

$$\tau = \frac{r-b}{c_w} \tag{16}$$

is the travel time from the source to a point at range r. The function F in (14) is

$$F(x) = \omega_s^2 \mathrm{Re}\left\{\frac{2\omega_1^2 \exp(j\omega_1 x)}{(\omega_1 + \omega_1^*)(\omega_1 - \omega_3)(\omega_1^2 - \omega_s^2)}\right\} + \omega_s^3 \mathrm{Re}\left\{\frac{\exp(j\omega_s x)}{(\omega_s - \omega_1)(\omega_s + \omega_1^*)(\omega_s - \omega_3)}\right\} - \frac{|\omega_s\omega_3|^2 \exp(-|\omega_3|\,x)}{|\omega_3 - \omega_1|^2\left(|\omega_3|^2 + \omega_s^2\right)} \tag{17}$$

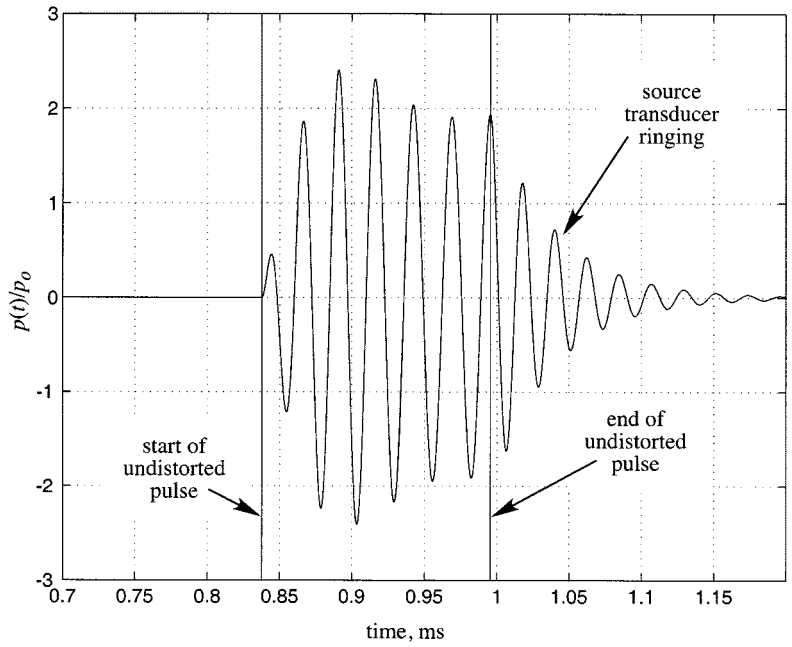

Fig. 3. Theoretical pressure-pulse shape in the water column, range 1.3 m, evaluated from (14) for operating conditions on Julian day 291, SAX99 (see text). The vertical lines indicate where the beginning and end of the pressure pulse would have fallen had there been no distortion from the source transducer.

where the asterisk denotes complex conjugate. Clearly, the expression for the received pressure pulse in (14) satisfies causality, since there is no arrival before $t = \tau$. It is also evident that, as (14) does not represent a sinusoidal tone burst, the transmitted pressure waveform is not a replica of the input voltage.

Fig. 3 shows an example of the theoretical pressure-pulse shape from (14) for a source-to-receiver range of $r = 1.3$ m and under the operating conditions prevailing on Julian day 291 (see Richardson *et al.* [1, Fig. 7]) in SAX99. On that occasion, the speed of sound in seawater was $c_w = 1537$ m/s, the density of seawater was $\rho_w = 1024$ kg/m^3, and the input pulse was a 6-cycle sinusoid at 38 kHz, as illustrated in Fig. 2(a). For reasons discussed below, the source transducer in seawater is taken to have a resonance frequency $\omega_{ow}/2\pi = 45$ kHz and $Q_w = 6$.

Several differences between the input pulse in Fig. 2(a) and the received pulse in Fig. 3 are obvious. Firstly, the received pulse is of extended duration, due to the ringing of the source transducer. Secondly, the maxima and minima in the pulse arrival have nonuniform amplitudes, in contrast with the constant level of the input; and thirdly, the zero crossings in the arrival are more densely packed than those in the input, indicating that phase shifting is occurring within the pulse. All these effects may be attributed to the resonant nature of the source transducer.

B. Measured Pulse Shapes

Fig. 4 shows two water-column pulses at nominal ranges of 1.300 and 0.298 m, as observed with ISSAMS on Julian day 291 of SAX99. The "nominal range" is the physical path length between the center of the source and nearest point on the receiver, as measured using a graduated rule. On comparing Figs. 3 and 4(a), it is clear that, detail by detail, the features of the theoretical and observed pulses are almost perfectly matched. The two pulses are offset slightly in time only because the actual acoustic path length between the source and receiver in the experiment was not precisely 1.300 m. Notice also that the pulse arrivals at the far [Fig. 4(a)] and near [Fig. 4(b)] phones are almost identical in shape, as expected since attenuation and dispersion in seawater under ISSAMS operating conditions are negligible.

The strong similarity between the theoretical prediction in Fig. 3 and the experimental observations in Fig. 4 indicates that the L–C–R equivalent circuit, with $Q_w = 6$ and $\omega_{ow}/2\pi = 45$ kHz, accurately represents the resonance behavior of the source transducer in seawater. These bandpass parameters were chosen because they give the "best" visual fit between the theoretical and measured waveforms in Figs. 3 and 4. Although no direct measurements of the source parameters are available, these values of the resonance frequency and Q are not inconsistent with the sensitivity of a similar transducer used in a receiving mode, as shown in Barbagaleta *et al.* [8, Fig. 2].

C. Inter-Receiver Distance Calibration

It is important to notice that the distortion introduced by the band-limited source is such that there is not a one-to-one relationship between the principal features (maxima, minima, and zeros) in the input [Fig. 2(a)] and the output (Fig. 3). It follows that, if some feature of the input, say the fourth peak, were used as a timing reference to calibrate the source-to-receiver distance, on the assumption that the arrival is a replica of the input, a significant timing error would be expected.

Such difficulties may be avoided by abandoning source-to receiver paths in favor of receiver-to-receiver propagation. In the inter-receiver technique, the two arrivals, being equally distorted by the source, have very similar shapes, as exemplified by the pulse arrivals shown in Fig. 4(a) and (b). With two such pulses, the travel time between receivers can be determined un-

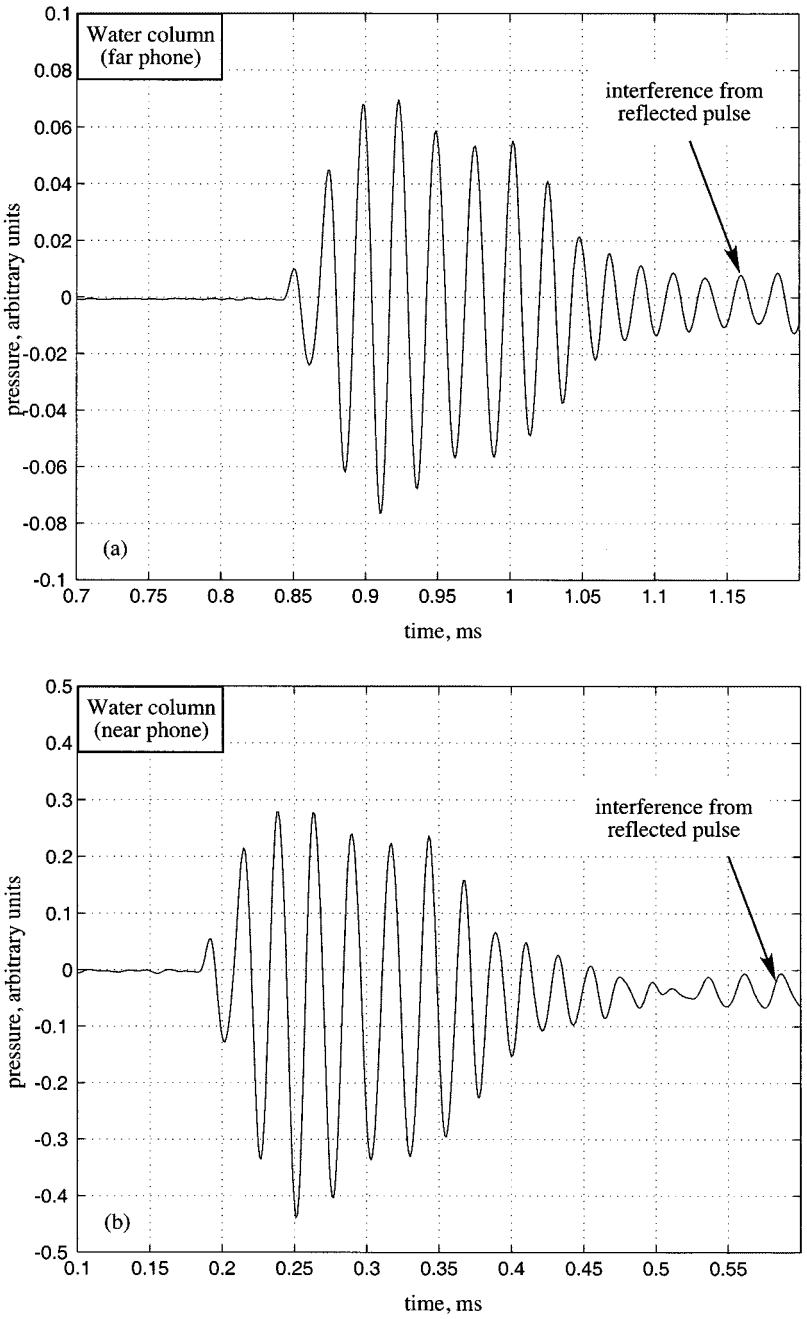

Fig. 4. Pressure-pulse shapes in the water column, as measured over nominal ranges of (a) 1.300 m ; (b) 0.298 m during Julian day 291, SAX99 (ISSAMS data file FWP544).

equivocally from a correlation analysis. The *inter-receiver correlation delay* immediately yields an acoustically calibrated distance, d_w, between receivers, given that the sound speed, c_w, in the water column is known.

Fig. 5 shows the (unnormalized) correlation function between the two water-column arrivals in Fig. 4. At the global maximum the inter-receiver correlation delay is $t_w = 0.659$ ms which, as the sound speed in the water column was $c_w = 1537$ m/s, yields an inter-receiver correlation distance $d_w = 1.013$ m. This is greater than the nominal distance between the receivers by 11 mm, or approximately 1.1%, but this disparity is comparable with the physical size of the transducers themselves and hence has little significance.

V. Pulses in the Sediment

Unlike seawater, a marine sediment exhibits noticeable frequency dispersion and attenuation. For such a medium, the real and imaginary parts of the complex sound speed, c, depend on frequency and the analytical solution for the shape of the received pressure pulse in (14) and (17) does not hold. In general, however, the pulse shape may be obtained from (10) by numerically evaluating the integral over frequency. To perform the integration, it is necessary to specify the source-transducer bandpass parameters ω_o and Q, which will differ from their seawater values because of the enhanced loading of the sediment. Also needed is the functional form of the complex sound speed, representing the dispersion and attenuation, which will depend

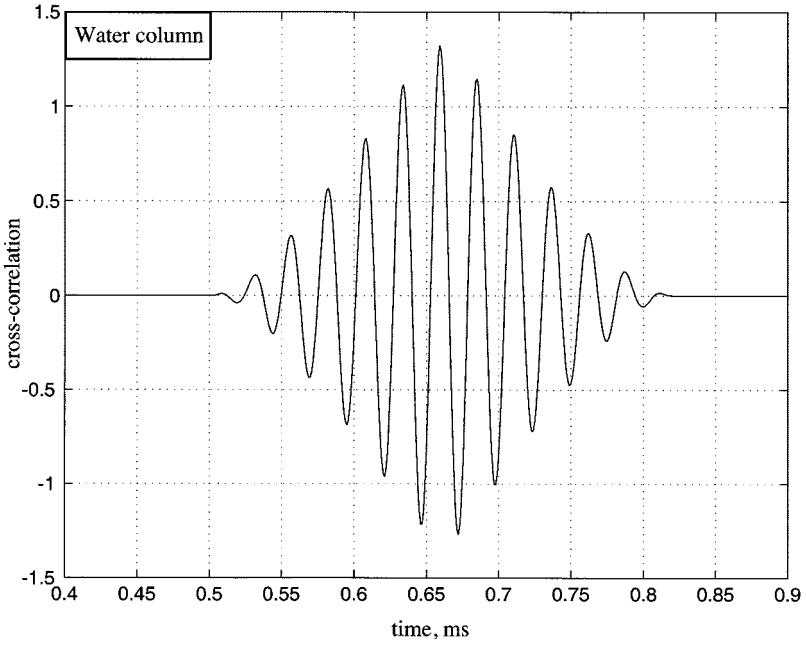

Fig. 5. Correlation function (unnormalized) between the water-column arrivals in Fig. 4. Zero padding was used to eliminate noise before and after the pulse arrivals.

on the theoretical model chosen to represent wave propagation in the granular medium.

A. Transducer Bandpass Parameters

The mass loading and radiation resistance of the medium are represented by the inductor, L_x, and resistor R_x, respectively, in the equivalent circuit of Fig. 1. These parameters will be higher in a sandy marine sediment than in seawater and the resonance frequency and the Q of the source transducer will be modified accordingly. From (3), the resonance frequency of the source transducer in the granular medium can be written as

$$\omega_{og} = \sqrt{\frac{L_m + L_{xw}}{L_m + L_{xg}}}\,\omega_{ow} \tag{18}$$

and similarly for the Q

$$Q_g = \left(\frac{R_m + R_{xw}}{R_m + R_{xg}}\right)\sqrt{\frac{L_m + L_{xg}}{L_m + L_{xw}}}\,Q_w \tag{19}$$

where the subscripts w and g denote "water" and "granular medium," respectively. The PZT ceramic used in the source transducer is a low-loss material with a Q in excess of 100, implying that $R_m \ll R_x$, from which it follows that (19) is well approximated as

$$Q_g \approx \frac{R_{xw}}{R_{xg}}\sqrt{\frac{L_m + L_{xg}}{L_m + L_{xw}}}\,Q_w. \tag{20}$$

To evaluate the scaling factors on the right of (18) and (20), the following expressions are used to estimate the equivalent circuit parameters. These expressions follow from Burdic [14]:

$$L_m = \tfrac{4}{3}\,\pi(b^3 - b_i^3)\rho_{PZT} \tag{21}$$

$$L_x = \frac{4\pi b\rho c_x^2}{\omega^2\left(1 + \frac{c_x^2}{\omega^2 b^2}\right)} \tag{22}$$

and

$$R_x = \frac{4\pi b^2\rho c_x}{\left(1 + \frac{c_x^2}{\omega^2 b^2}\right)} \tag{23}$$

where $b_i = 10.9$ mm is the internal radius of the source, $\rho_{PZT} \approx 5\rho_w$ is the density of the ceramic, and c_x is the sound speed in the medium (either seawater or sediment, as appropriate). The expression in (21) follows from Burdic [14, p. 62] but is a factor of two greater than Burdic's because the bar transducer considered in [14] is clamped at one end; and (22) and (23) follow from [14, p. 50].

To find ω_{og} from (18), $\omega = \omega_{og}$ is needed in (22). Instead, we use the initial value $\omega = \omega_{ow}$ in (22) and find ω_{og} by iteration. Taking $\omega_{ow}/2\pi = 45$ kHz, $\rho_g \approx 2\rho_w$ and $c_g = 1.16c_w$, the above expressions then yield $\omega_{og}/2\pi \approx 38$ kHz and $Q_g \approx 3$. Thus, according to this calculation, the resonance frequency of the source in the sediment is lower than that in the water column by a factor of approximately 0.84, with the pass band centered on 38 kHz, which matches the frequency of the transmitted pulses. In fact, this is a design feature of ISSAMS, which achieves optimum transmission performance of the 38 kHz pulses when the source is mass-loaded by a saturated sand. Note that the Q of the source in the sediment is estimated to be half that in seawater, signifying that the ringing at the trailing edge of the received pulse should be noticeably less pronounced in the sediment arrivals.

B. Dispersion and Attenuation

The complex sound speed, c, of a compressional wave in any linear dispersive material (not only granular media) can be expressed as

$$\frac{\omega}{c} = \frac{\omega}{c_g} - j\alpha_g \tag{24}$$

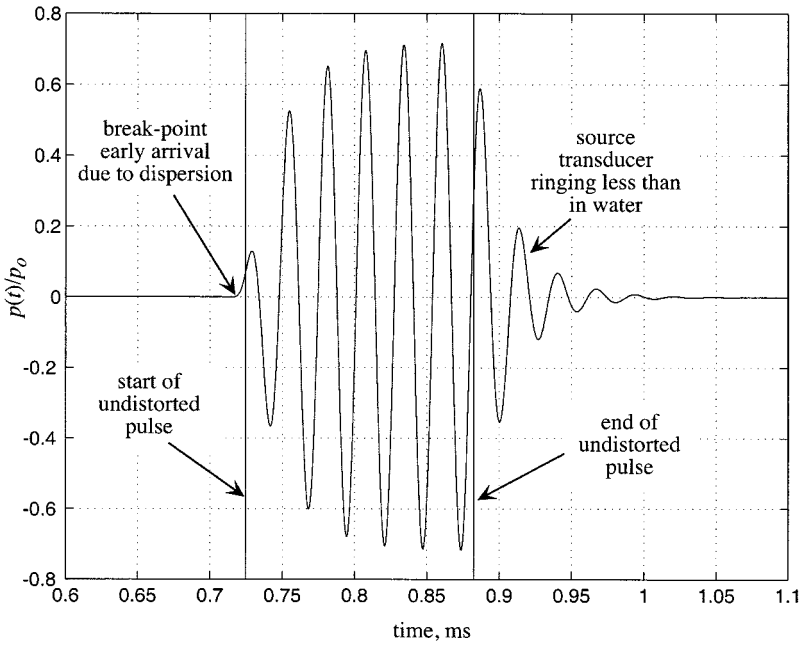

Fig. 6. Theoretical pressure-pulse shape in sediment, at range 1.3 m, evaluated from (10). The vertical lines indicate where the beginning and end of the pulse would have fallen had there been no dispersion or attenuation in the medium, and no distortion from the source transducer.

where c_g is the phase speed and α_g is the attenuation coefficient. In general, both parameters depend on frequency. Around the operating frequency of ISSAMS, considerable experimental evidence has accumulated over the past few decades which indicates that, in a saturated sediment, the dispersion is weak and the attenuation scales linearly, or nearly so, with frequency [11].

To evaluate the pressure-pulse integral in (10), theoretical expressions are required for c_g and α_g. Such expressions are available from Biot's classic theory of wave propagation in porous media [15], [16] in which the dissipation mechanism is viscosity of the pore fluid. Biot's result for the complex speed of the compressional wave is well fitted empirically by the form

$$\frac{1}{c} = \left(\frac{1}{c_o} - \frac{1}{c_\infty}\right)\left[\frac{1 - j\omega\gamma}{1 + \omega^2\gamma^2}\right]^{1/2} + \frac{1}{c_\infty} \qquad (25)$$

where (c_o, c_∞) are the phase speeds in the limit of low and high frequency, and the coefficient γ scales inversely with the effective kinematic viscosity. Note that, if c_∞^{-1} were allowed to vanish, (25) would reduce identically to the functional form for the complex sound speed in a true viscous fluid. The condition $\omega\gamma = 1$ identifies a transition frequency, which separates the low- and high-frequency regimes in the Biot formulation of the complex wave speed in (25). At lower frequencies, the attenuation scales as ω^2 but, beyond $\omega \approx 1/\gamma$, the power law changes to $\omega^{1/2}$.

From the formulation in (25), it is evident that the Biot model for the complex speed of the compressional wave has just three degrees of freedom, represented by the three *independent* parameters (c_o, c_∞, γ). Thus, it is more tightly constrained than is often implied in the literature [17], [18], where the Biot model is discussed in terms of thirteen parameters. Of course, the three parameters in (25), which uniquely characterize the Biot model, can themselves be expressed in terms of the thirteen Biot parameters, which would be necessary if the model were to be used for predictive purposes. However, to establish whether the Biot predictions match the shapes of the sound speed and attenuation data, (25) is a satisfactory and convenient representation. As an example of the functional form of the Biot predictions, see the solid-line plots of sound speed (ratio) and attenuation in Williams *et al.* [19, Figs. 3 and 4], which, with a sound speed in water of $c_w = 1537$ m/s, are reproduced by (25) with $c_o = 1665$ m/s, $c_\infty = 1794$ m/s and $\gamma = 0.17$ ms.

The double-power law predicted by the Biot theory for the frequency dependence of the attenuation (scaling as ω^2 below the transition frequency and $\omega^{1/2}$ above) is not characteristic of the broadband (10 to 100 kHz) data sets that were acquired with ISSAMS during SAX99. The disparities between the Biot predictions and the attenuation data, discussed later in Section XI, are illustrated pictorially in Figs. 20(b) and 21(b). An alternative to the Biot theory was proposed recently by Buckingham [20], in which the dispersion and dissipation arise from inter-granular traction. According to this model, the complex sound speed may be expressed as follows:

$$\frac{1}{c} = \frac{1}{c_o}\left[1 + \eta(j\omega T)^n\right]^{-1/2} \qquad (26)$$

where the stress-relaxation exponent, n, is a small, positive number ($0 < n \ll 1$), η is a dimensionless constant representing the effect of grain-to-grain interactions, and $T = 1$ s is a normalizing time, introduced solely to ensure that the term raised to the fractional power n remains dimensionless. Like the expression in (25) representing the Biot theory, (26) is tightly constrained, with only three degrees of freedom, represented by the three independent parameters (c_o, η, n). The predicted dispersion is weakly logarithmic, of the order of 1% per decade of frequency, and the attenuation is essentially proportional to the first power of frequency over many decades. These trends are consistent with many of the experimental

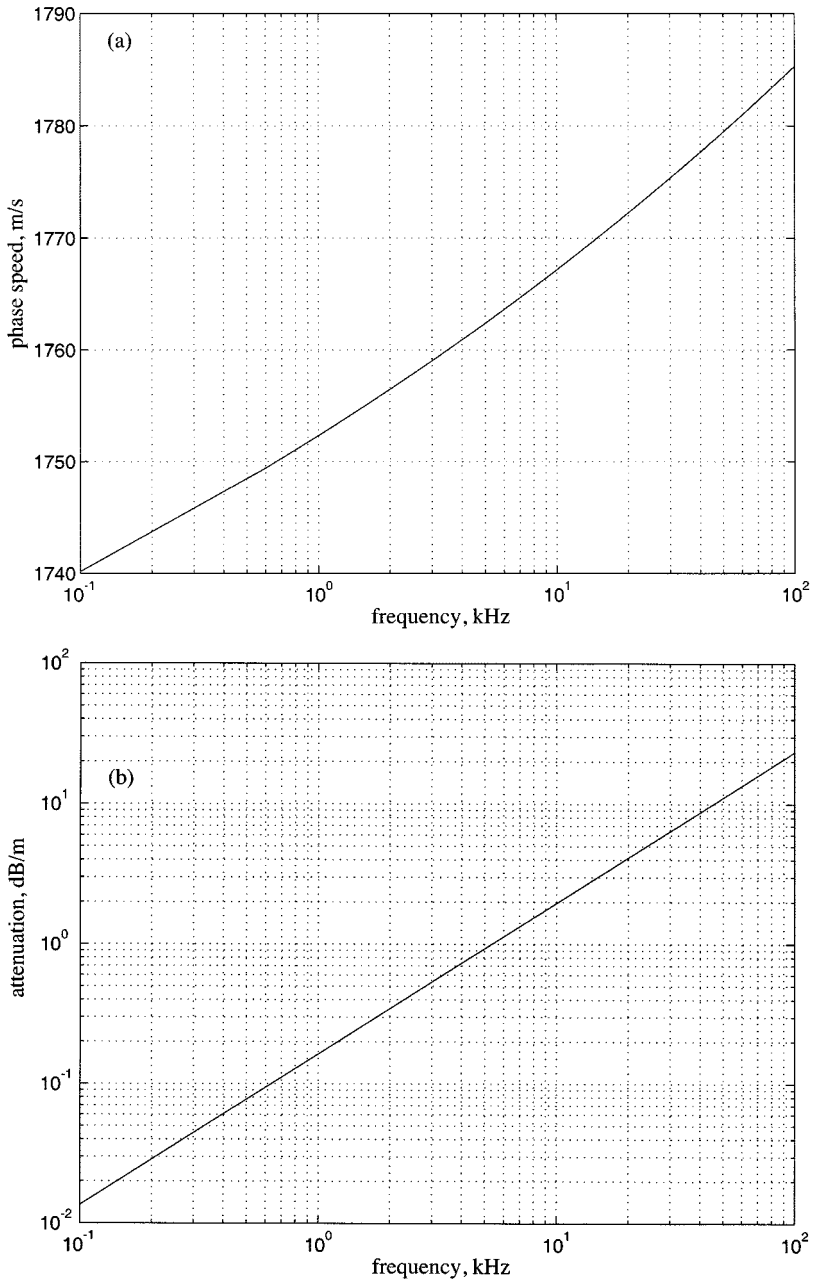

Fig. 7. Theoretical (a) dispersion; (b) attenuation in the sediment, from (26).

measurements of dispersion and attenuation in marine sediments that have been reported in the literature in recent years, as reviewed by Buckingham [20]. Moreover, the near-linear scaling of attenuation with frequency that emerges from (26) matches several of the broadband attenuation data sets acquired during SAX99, including those reported by Williams *et al.* [19] over the frequency range from 11 to 400 kHz, and also the measurements from ISSAMS shown in Figs. 20(b) and 21(b). For these reasons, (26) is used below in the computation of the pressure-pulse integral in (10).

C. Theoretical Pressure Pulses in the Sediment

An example of a pressure pulse from (10), evaluated using a Simpson's rule algorithm, is shown in Fig. 6. In performing the computation, the nominal source-to-receiver range was taken as 1.3 m, the grain-traction parameter and the stress-relaxation exponent, respectively, were assigned the values $\eta = 0.0365$ and $n = 0.09$, and the low-frequency sound speed was set to $c_o = 1686.5$ m/s. With these values for the sediment parameters, the theoretical dispersion and attenuation curves, evaluated from the real and imaginary parts of (26), are shown in Fig. 7. The resonance frequency of the source transducer was set at $f_{og} = 38$ kHz, with $Q_g = 3$, as estimated above for the source transmitting into a sediment. [*N.B.* The beginning and end of the "undistorted" pulse depicted in Fig. 6 were calculated by treating the sediment as dispersionless with a sound speed of 1777 m/s, which is the theoretical value in Fig. 7(a) at the ISSAMS pulse frequency of 38 kHz.]

It is instructive to compare the theoretical pulse shapes in Figs. 3 and 6 for the water and sediment, respectively. The be-

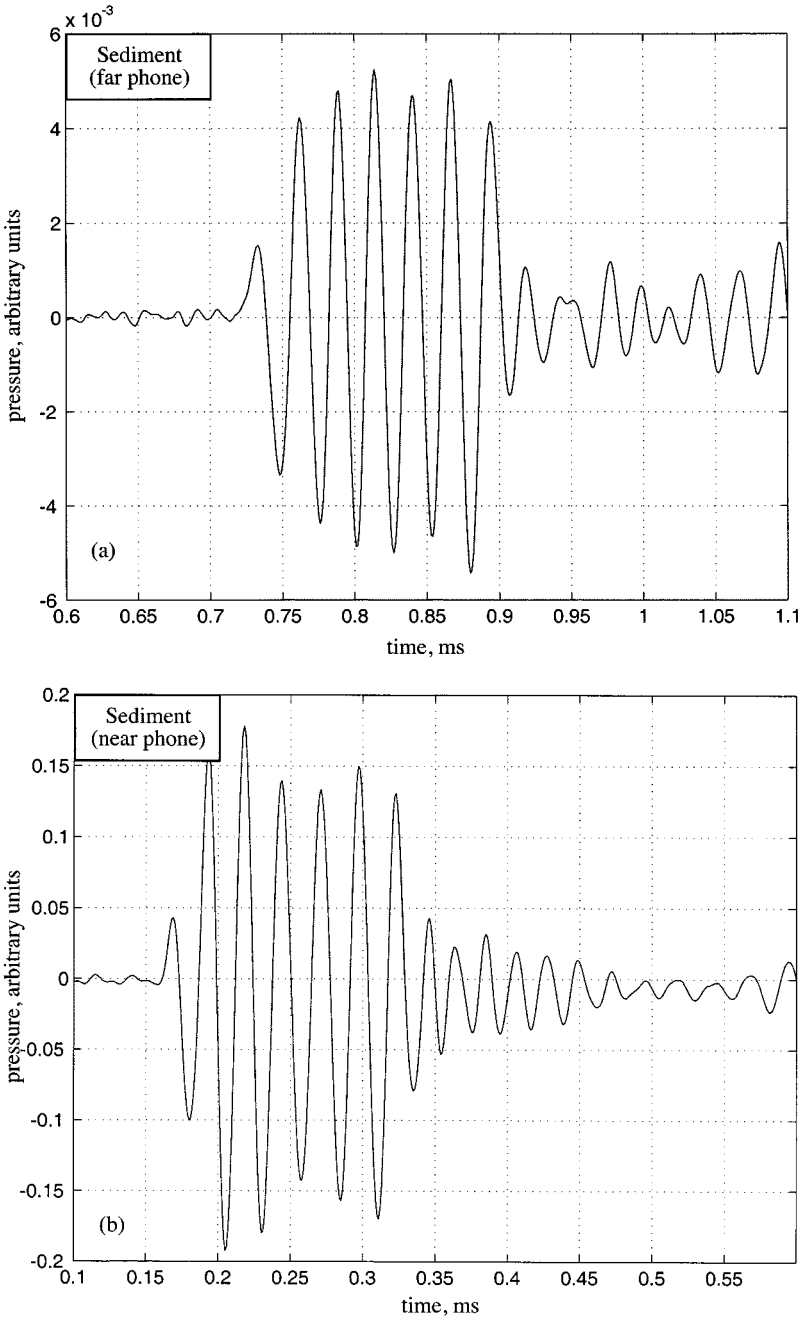

Fig. 8. Pressure-pulse shapes at a depth of 30 cm in the sediment, as measured over nominal ranges of (a) 1.300 m ; (b) 0.298 m during Julian day 291, SAX99 (ISSAMS data file FWP541).

ginning of the leading edge, or break point, is where the pressure initially departs from zero. In the water-borne arrival in Fig. 3, the break point coincides with the start of the undistorted pulse, that is to say, the bandpass nature of the source in a dispersionless medium does not affect the arrival time of the break point. This being so, the break point could be used as a timing marker, as an alternative to the correlation function in Fig. 5. In contradistinction, the break point of the sediment-borne pulse in Fig. 6 arrives in advance of the undistorted pulse, because of dispersion. Being a relatively sharp feature, the break point is governed by the higher Fourier components in the pulse, which, in the sediment, travel faster than the center frequency component (38 kHz), and thus the break point arrives ahead of the dispersionless, undistorted pulse. It follows that, in the dispersive sediment, the break point would be an unsatisfactory timing marker. At the trailing edge of the pulse, the ringing in Figs. 3 and 6 is characteristic of the different Q-factors in the two media: the ringing in the sediment pulse ($Q_g = 3$) is noticeably suppressed relative to that in the water pulse ($Q_w = 6$).

Fig. 8 shows two pressure-pulse arrivals, as measured with ISSAMS, at a depth of 0.3 m in the sediment and over nominal ranges of 1.300 and 0.298 m, on Julian day 291, SAX99. It is clear from a visual comparison of Fig. 8(a) with Fig. 6 that the detailed features of the measured pulse are very similar to those of the theoretical prediction. The theoretical and observed pulses are offset slightly in time because the range was not pre-

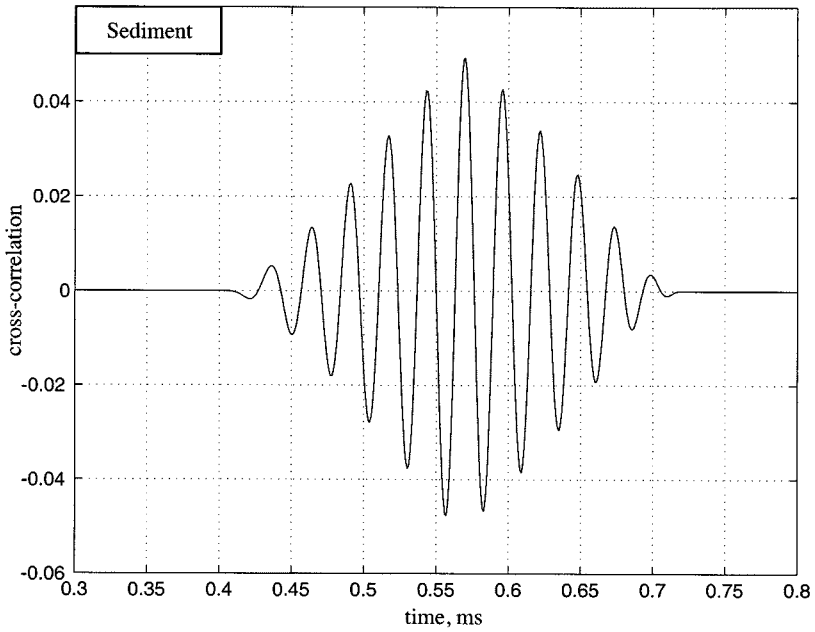

Fig. 9. Correlation function between the two sediment arrivals in Fig. 8. Zero-padding was used to suppress noise before and after the pulse arrivals. The distance between the two receivers, as calibrated acoustically from the correlation delay in the water column, was $d_w = 1.013$ m.

cisely 1.300 m in the measurement set-up. Notice that, as with the theoretical pulses in Figs. 3 and 6, the ringing at the trailing edge of the measured sediment pulses in Fig. 8 is less than that in the measured water-borne pulses in Fig. 4, because of the lower Q of the source transducer in the granular medium.

D. Inter-Receiver Correlation Timing for the Group Speed

As in the water column, the inter-receiver correlation technique may be applied to the arrivals at two receivers in the sediment, to obtain the travel time from one to the other. The correlation function between the two sediment pulses in Fig. 8 is shown in Fig. 9, where the delay at the global maximum is $t_s = 0.570$ ms. From the seawater calibration, the distance between the receivers is $d_w = 1.013$ m, and thus the estimated wave speed is 1777 m/s at the pulse frequency of 38 kHz.

In SAX99, the timing resolution of ISSAMS was 1 μs, yielding travel-times that are accurate to within 0.2%. Since travel time is measured twice in the estimate of the wave speed, once in the seawater, inter-receiver distance calibration and again over the receiver-to-receiver path in the sediment, the total intrinsic measurement error in the estimates of the wave speed is of the order of $\sqrt{2} \times 0.2 \approx 0.3\%$. Thus, the intrinsic error in the wave speed estimates is approximately ± 5 m/s. An improvement by a factor of ten in the timing resolution, with a corresponding increase in the accuracy of the estimated wave speeds, is planned for a future variant of ISSAMS.

When used with a dispersive material, the inter-receiver correlation-timing technique yields a good approximation to the group speed. With the relatively narrow-band tone bursts used in ISSAMS, and bearing in mind that the dispersion in the sediment is weak at approximately 2% per decade of frequency, the difference between the group speed and the phase speed is negligible. It is worth noting, however, that if any spurious component, such as a sharp switching spike, were present in the transmitted pulse, then the correlation technique may return an incorrect wave speed. The correlation time could be governed by the arrival of the spike, which, because of its higher frequency content, travels at a different speed from the pulse itself. In the case of a sediment, where the phase speed is monotonic increasing with frequency, this could lead to an over-estimate of the wave speed. For this reason, it is important to remove high-frequency artifacts from the received pulses, either by filtering or zero-padding of the arrivals.

VI. Phase-Delay Timing

Like the tone-burst input signal, the received acoustic pulses contain frequency components on either side of the center frequency. The frequency spread is illustrated in Fig. 10, which shows the power spectrum of the water column arrivals in Fig. 4, as measured with ISSAMS during SAX99. The input pulse in this case was a 6-cycle, 38 kHz sine wave of the form shown in Fig. 2(a). It is evident that most of the energy in the received pulses lies in the frequency band between 34 and 44 kHz, with the peak energy occurring at approximately 39 kHz. This peak frequency is slightly higher than the center frequency of the input pulse because of the offset pass band of the source transducer in seawater, which is centered on 45 kHz. Fig. 11 illustrates the power spectra of the sediment arrivals shown in Fig. 8. Most of the energy in this case falls between 34 and 42 kHz, with the peak at 38 kHz, which is expected because, in this sediment, the resonance frequency of the source coincides with the center frequency of the input pulse. Notice that the ratio of the spectral levels at the far and near receivers is orders of magnitude less in the sediment than in the water column because of the relatively high attenuation in the granular medium.

At each frequency in the spectrum, the phase delay between receivers may be used to estimate the travel time in the sediment, from which the phase speed as a function of frequency is

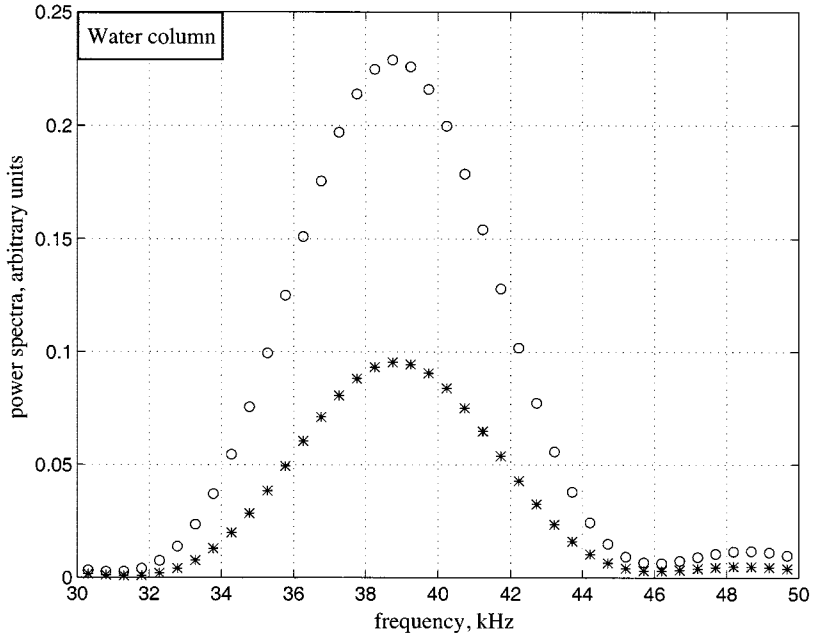

Fig. 10. Power spectra of the water-column pressure-pulse arrivals in Fig. 4. The open circles (∘) represent the near receiver (nominal range 0.298 m) and the asterisks (∗) the far receiver (nominal range 1.3 m). For clarity of presentation, the latter levels have been scaled up by a factor of 10.

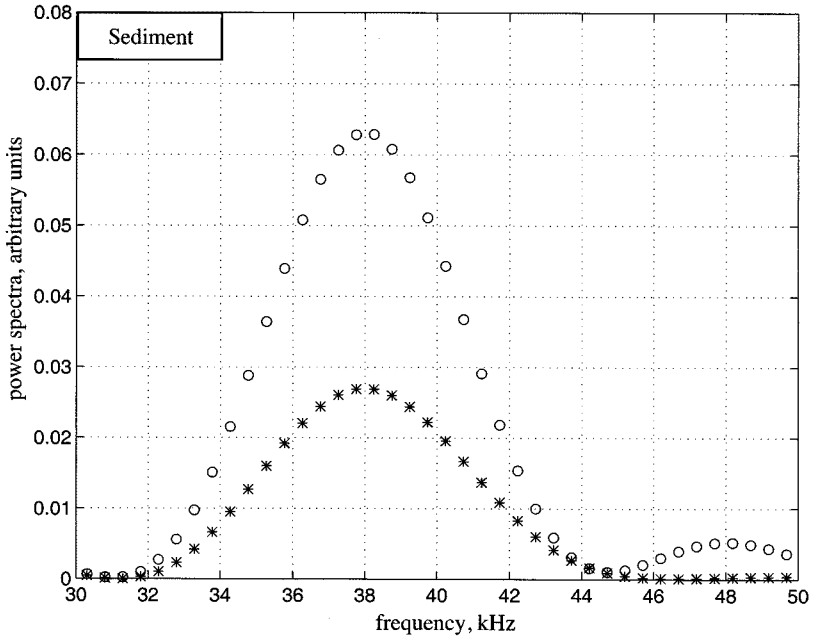

Fig. 11. Power spectra of the sediment pressure-pulse arrivals in Fig. 8. The open circles (∘) represent the near receiver (nominal range 0.298 m) and the asterisks (∗) the far receiver (nominal range 1.3 m). For clarity of presentation, the latter levels have been scaled up by a factor of 500.

derived, assuming that the sensor separation is d_w, the value obtained from an acoustic calibration in the water column. Fig. 12 shows the (wrapped) phase delay, $\Delta\phi_p$, between these two arrivals in the range $[-\pi\ \pi]$. The four-quadrant phase is defined as

$$\Delta\phi_g = \tan^{-1}\left\{\mathrm{Im}(P_{1g}/P_{2g}), \mathrm{Re}(P_{1g}/P_{2g})\right\} \qquad (27)$$

where P_{1g} and P_{2g} are the Fourier transforms of the pressure-pulse arrivals in the sediment at the far and near receiver, respectively. The discontinuities that can be seen in the phase in Fig. 12 occur because the number of complete wavelengths between the two receivers is incremented by one at these frequencies.

Phase unwrapping is performed by adding $2\pi v$ to the phases in Fig. 12, where the wrapping number, v, is an integer which increases by one at frequencies where the (wrapped) phase discontinuities occur. The compressional wave speed in the sediment is then given by

$$c_p = \frac{\omega d_w}{[2\pi v + \Delta\phi_p]} \qquad (28)$$

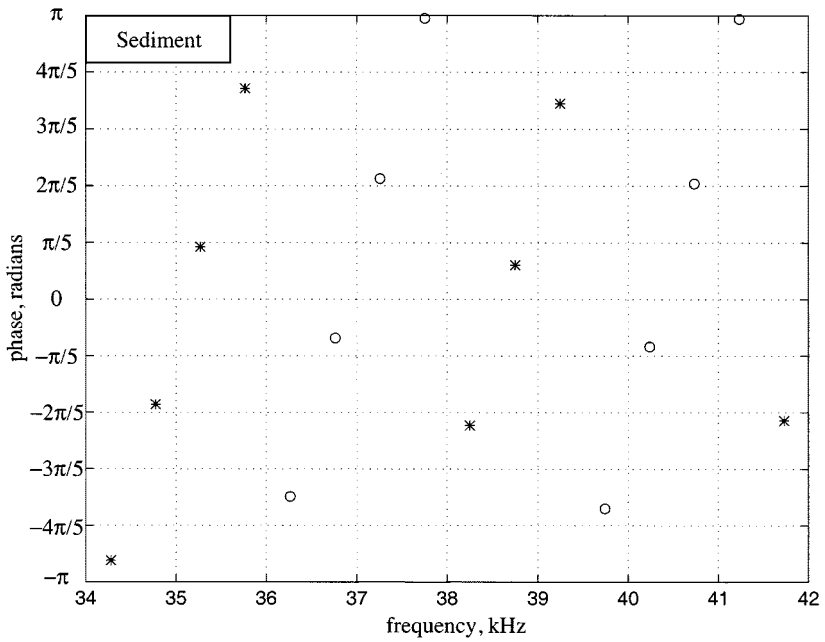

Fig. 12. Four-quadrant phase delay between the two sediment pressure-pulse arrivals in Fig. 8. On passing through a discontinuity in the phase, the symbol changes from an asterisk to an open circle or *vice-versa*.

where d_w is the water column acoustic calibration distance between receivers. A straightforward way to determine v at each frequency is to exploit the expected similarity between the group speed and phase speed in the weakly dispersive sediment. The appropriate wrapping number is the one for which the phase speed computed from (28) is closest to the group speed determined from the inter-receiver correlation. The wrapping number determined using this comparative approach returns phase speeds that are usually within 3 m/s of the group speed, as exemplified by the data in Table I.

For the five phase segments in Fig. 12, v takes integer values from 20 to 24. When these values are substituted into (28), with $d_w = 1.013$ m, the wave speeds shown in Fig. 13 are obtained. The mean of the phase-delay wave speeds is 1778.6 m/s, just 1.4 m/s higher than the inter-receiver-correlation delay estimate of 1777.2 m/s, a negligible disparity which falls within the measurement error of ± 5 m/s for the correlation technique.

The measurements of wave speed using the phase-delay technique are sensitive to the start time of the window applied to the pulse arrivals. By repeatedly running the phase-delay algorithm over a sequence of start times spanning a full wave period in increments of 1 μs, the fluctuations in the estimated wave speed were found to fall within an interval of approximately ± 5 m/s, which is the same as the inherent error on the correlation-delay estimates. Given its relative ease of computation, the inter-receiver correlation-delay method is recommended for narrow-band tone bursts such as those used in ISSAMS. With broader-band pulses, however, the inter-receiver phase-delay technique could be a preferable choice.

VII. Source-to-Receiver Cross-Correlation Timing

Richardson [10] used a cross-correlation technique to measure the *difference*, Δt, between the source-to-receiver travel times in seawater and the underlying sediment. The distance, d_x, between the source and receiver was calibrated acoustically in seawater of known sound speed, c_w, by estimating the travel time from the leading edge of the waveform, or breakpoint, where the pressure initially departs from zero. The sound speed, c_g, in the sediment was then computed from the following expression [10]:

$$c_g = \frac{c_w}{1 - \frac{c_w \Delta t}{d_x}}. \tag{29}$$

Besides the intrinsic timing error from the sampling rate, there is a potential source of systematic error in this technique. It is in the *cross-correlation delay* Δt, and occurs because the received signals in the sediment and the water column are not the same shape. They differ because the arrival in the sediment is modified by dispersion and attenuation, and also because the bandpass parameters of the source are different in the two media. In principle, a second systematic error may also be present, arising from the difficulty of selecting the break point in the water-borne arrival in the presence of a finite signal/noise ratio. This will affect the estimate of d_x but the magnitude of the error is usually negligible. An interesting feature of (29) for estimating c_g is that the percentage error in Δt acts on the *difference* between the sound speeds in water and the sediment, rather than on c_g itself and thus, even for the relatively high-speed sediments in SAX99, the resultant error in c_g is reduced by about 5 : 1. Nevertheless, this systematic error may still be significant and was the source of the spurious range-dependent sediment sound speeds obtained from the preliminary analyzes of the SAX99 data.

VIII. Inter-Receiver Attenuation

The acoustic attenuation in the sediment may be determined by forming the ratio of either the spectral amplitudes or the mean-square levels of the pulse arrivals at the two receivers in

TABLE I
(a) SERIES *9B* SOUND SPEED AND ATTENUATION DATA FROM CROSS-CORRELATION (c×), MEAN-SQUARE ($\alpha\times$) AND FOURIER (cf., αf). (b) SERIES *13B* SOUND SPEED AND ATTENUATION DATA FROM CROSS-CORRELATION (c×), MEAN-SQUARE ($\alpha\times$) AND FOURIER (cf., αf)

(a)

file#wat/sed	freq., kHz	cx, m/s	αx, dB/m	cf, m/s	αf, dB/m
289/235	25	1773	10.43	1773	8.565
290/236	30	1779	9.172	1778	10.12
291/237	35	1779	7.891	1783	10.38
292/238	40	1791	10.08	1789	9.608
293/239	45	1774	13.62	1777	13.36
294/240	50	1785	14.83	1786	15.63
295/241	55	1780	15.12	1786	15.68
296/242	60	1785	16.49	1784	16.32
297/243	65	1785	18.82	1784	19.22
298/244	70	1785	21.78	1784	21.94
299/245	75	1779	22.25	1784	22.52
300/246	80	1790	24.16	1788	25.02
301/247	85	1784	26.43	1781	26.44
302/248	90	1790	26.92	1786	27.26
303/249	95	1784	27.82	1786	28.48
304/250	100	1784	29.27	1787	30.93

(b)

file#wat/sed	freq., kHz	cx, m/s	αx, dB/m	cf, m/s	αf, dB/m
411/363	25	1773	14.65	1772	14.79
412/364	30	1779	16.72	1776	16.55
413/365	35	1779	18.52	1778	17.92
414/366	40	1780	24.3	1782	23.96
415/367	45	1786	27.06	1785	27.49
416/368	50	1791	28.48	1792	28.69
417/369	55	1791	29.34	1793	29.72
418/370	60	1796	32.11	1795	32.16
419/371	65	1796	34.13	1795	34.44
420/372	70	1796	37.96	1793	38.79
421/373	75	1796	40.72	1795	41.52
422/374	80	1790	43.65	1794	43.82
423/375	85	1790	46.87	1793	46.94
424/376	90	1795	51.53	1791	51.83
425/377	95	1790	54.18	1790	54.45
426/378	100	1790	59.11	1791	60.52

the sediment. However, a water-column calibration is necessary in order to eliminate any mismatch in the amplitude response of the receivers, as well as to remove the effects of geometrical spreading. By backing out the latter, no particular form of spreading law need be assumed. The only implicit assumptions are that the geometrical spreading is the same in the water column as in the sediment, and that any change in the frequency response characteristics of the two receivers as they are moved from seawater to sediment should be the same on both.

A. Spectral Amplitudes

The (far/near) spectral ratio of the two pulses in the water column is

$$A_w(\omega) = \left| \frac{P_{1w}(j\omega)}{P_{2w}(j\omega)} \right|^2 \tag{30}$$

which serves as the amplitude calibration, taking account of geometrical spreading and any amplitude mismatch between the receiver responses. At frequencies around 38 kHz, attenuation in seawater is predominantly due to the ionic relaxation of magnesium sulfate, but this is of the order of 0.01 dB/m, which is far too weak to have a significant effect on the spectral ratio in (30). For practical purposes, seawater may be regarded as lossless.

The (far/near) spectral ratio of the pulses in the sediment is

$$A_g(\omega) = \left| \frac{P_{1g}(j\omega)}{P_{2g}(j\omega)} \right|^2 \tag{31}$$

which includes the effects of geometrical spreading, amplitude mismatch of the receivers, and attenuation in the granular

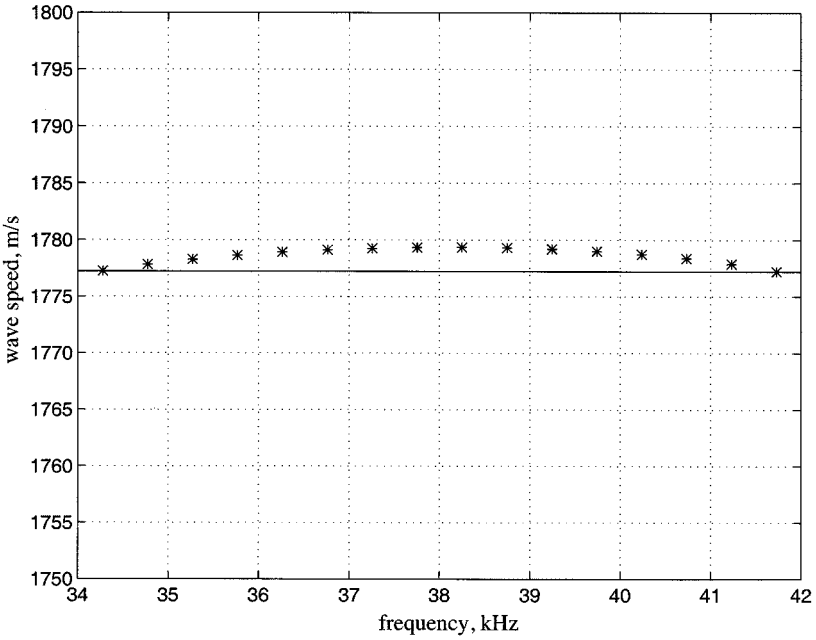

Fig. 13. Wave speed at 30-cm depth in the sediment as a function of frequency, as estimated from the pulses in Fig. 8. The asterisks ($*$) were computed from (28) and the solid line is the wave speed estimated from the inter-receiver correlation delay between the pulse arrivals.

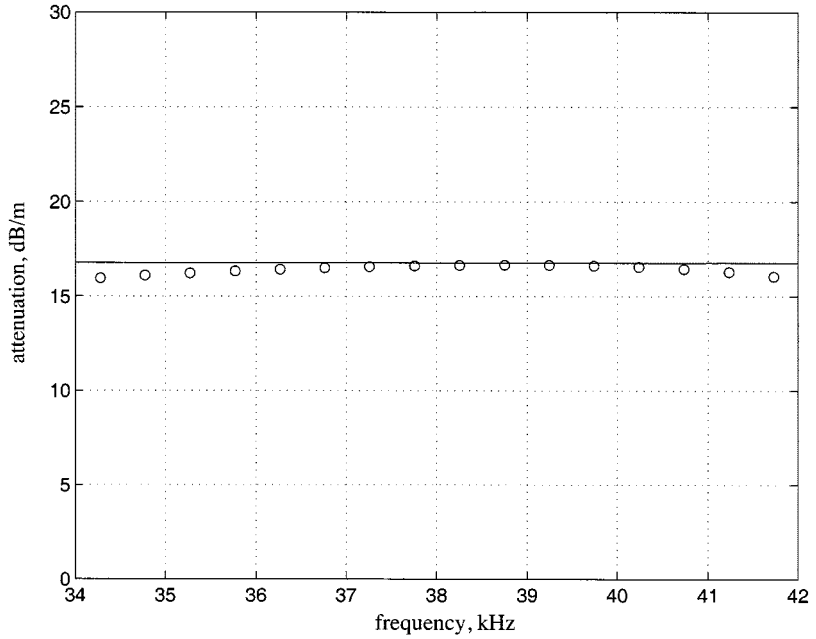

Fig. 14. Attenuation as a function of frequency at a depth of 30 cm in the sediment, estimated from the pressure-pulse arrivals in Fig. 8. The open circles were computed from the power spectra of the pulses using (32), and the solid line is the attenuation estimated from the mean-square values of the two pulses, (35).

medium. The attenuation coefficient of the sediment, α_g, is obtained from (30) and (31) as

$$\alpha_g(\omega) = \frac{1}{2d_w} \ln\left\{\frac{A_w(\omega)}{A_g(\omega)}\right\}. \tag{32}$$

[*N.B.* As expressed in (32), the attenuation is in nepers per unit distance, which should be multiplied by $20\log(\exp(1)) \approx 8.686$ to convert to dB per unit distance.] For the two sediment pulses in Fig. 8, $A_w(\omega)$ and $A_g(\omega)$ are the ratios of the spectral pairs in Figs. 10 and 11, respectively. Using the water-calibrated, inter-receiver correlation distance $d_w = 1.013$ m, (32) returns the attenuation versus frequency depicted by the open circles ($\circ$) in Fig. 14.

In Fig. 14, the errors on the estimates of attenuation derived from spectral amplitudes arise mainly from the windowing of the pulse arrivals at the two receivers. Although the timing resolution of 1 μs introduces an error of approximately 0.2% into the estimate of the distance between the receivers, this is negligible compared with the effect of the windowing. To arrive at an estimate of the windowing error, the spectral amplitude algorithm was repeatedly applied to the data, with the start time of a window cycled in increments of 1 μs through a complete

wave period. The attenuation was found to vary by approximately ± 0.75 dB/m, which, across the band shown in Fig. 14, partially masks any reasonable frequency dependence that the attenuation may be expected to possess. Additional errors may also be present in the spectral amplitude technique, especially at frequencies away from the center of the pulse spectrum, where the signal-to-noise ratio is poor.

B. Mean-Square Levels

The attenuation may also be estimated from the mean-square values of the pulses in Figs. 4 and 8, yielding a frequency-independent value, which, in effect, is an average of the attenuation over the bandwidth of the pulse. If the (far/near) ratio of the mean-square values of the pulses in the water column is

$$B_w = \frac{\langle p_{1w}^2(t)\rangle}{\langle p_{2w}^2(t)\rangle} \tag{33}$$

and the corresponding ratio in the sediment is

$$B_g = \frac{\langle p_{1g}^2(t)\rangle}{\langle p_{2g}^2(t)\rangle} \tag{34}$$

where the symbol $\langle\cdots\rangle$ denotes a time average over the pulse length, then the attenuation can be expressed in nepers per unit distance as

$$\alpha_g = \frac{1}{2d_w}\ln\left(\frac{B_w}{B_g}\right). \tag{35}$$

For the sediment pulses in Fig. 8, this expression yields an attenuation $\alpha_g = 16.77$ dB/m, which is shown as the solid line in Fig. 14.

The mean-square technique for estimating attenuation is slightly more robust to windowing effects than the spectral amplitude method, but such effects are still the main source of measurement error. Again by cycling through the same sequence of windows, the attenuation returned by the mean-square technique was found to vary by approximately ± 0.5 dB/m.

As can be seen in Fig. 14, the spectral amplitude and mean-square techniques for estimating the attenuation return essentially the same value of approximately 17 dB/m at 38 kHz for the SAX99 medium-sand sediment at the center frequency of the pulse. This value is comparable with the attenuation reported for marine sands by other investigators, notably Hamilton [11], [12] and Richardson [13]. Both methods are reasonably easy to compute but there would be an advantage in using the spectral ratio technique with broadband pulses, since it returns directly the frequency-dependence of the attenuation across the band.

IX. Attenuation From Transposition

Richardson [10] introduced a transposition technique for measuring the attenuation in sediment. Two sources and two receivers are used, with the receivers located in the sediment between the sources. The distances between the transducers are obtained from seawater, source-to-receiver calibrations. An important advantage of the transposition technique is that mismatches in receiver sensitivity and insertion losses are automatically backed out of the estimate of the attenuation. The main assumption is that the transmitted signals undergo spherical spreading.

Using the terminology defined in Richardson [10, Fig. 1], the attenuation coefficient, in nepers/m, is

$$\alpha_t = \frac{1}{2d_2}\ln\left[\left(\frac{d_1}{d_1+d_2}\right)\left(\frac{d_3}{d_2+d_3}\right)\left(\frac{e_{1a}e_{2b}}{e_{2a}e_{1b}}\right)\right] \tag{36}$$

where d_i, $i = 1, 2, 3$, are the three distances defined in [10] between the four transducers and the four e parameters are the peak outputs from the two receivers with one or other of the transmitters operating. The transposition technique will be used later to evaluate the sediment attenuation at the SAX99 site.

X. Re-Analysis of the 38 kHz Wave Speed and Attenuation Data From SAX99

During SAX99, ISSAMS was deployed at the Fort Walton Beach site to make compressional wave speed and attenuation measurements at six (6) primary stations, numbered 2, 3, 4, 7, 9, and 13, and two (2) additional stations, numbered 15 and 23. At the primary stations, the measurements were performed at three depths in the sediment, 10, 20, and 30 cm, and at just the one depth of 30 cm at the additional stations.

A. Source-to-Receiver Sound Speed Measurements

The source-to-receiver measurements at the primary stations returned a mean sound speed, from (29), of 1744 m/s, with spread between 1691 and 1791 m/s, and a mean attenuation, from (36), of 15.7 dB/m, with spread between 8.6 and 26.1 dB/m. In both cases, the averaging was performed over all three depths. The spread in both sets of measurements is indicative of the variability that was observed, which is typical of sandy substrates [13], [21]. However, the sound speeds showed a trend toward a systematic dependence on the path length, with the longer distances returning faster speeds. For example, with transducer spacings of 0.35 m and 0.90 m, the mean sound speeds were found to be significantly different (t-test > 0.1) with values 1725 and 1753 m/s, respectively.

In an effort to resolve the issue of the spurious path-length dependence, an additional ten deployments of ISSAMS were made over a two-day period at stations 15 and 23, with source-to-receiver separations between 10 and 130 cm. (Stations 15 and 23 are actually the same site, with the numbers representing deployments on different days.) From (29), using cross-correlation timing between source and receiver, this new data set yielded a mean sound speed of 1753 m/s (S.D. $= 19.5$ m/s), with a spread between 1702 and 1781 m/s. Again, however, the estimated wave speeds exhibited a conspicuous dependence on range. This tendency toward higher estimated sound speeds at longer distances is illustrated in Fig. 15(a), which shows the computed sound speed as a function of source–receiver distance for stations 15 and 23.

B. Inter-Receiver Sound Speed Measurements

The compressional wave data collected with ISSAMS during the 10 deployments at stations 15 and 23 were re-examined using the inter-receiver speed and attenuation measurement

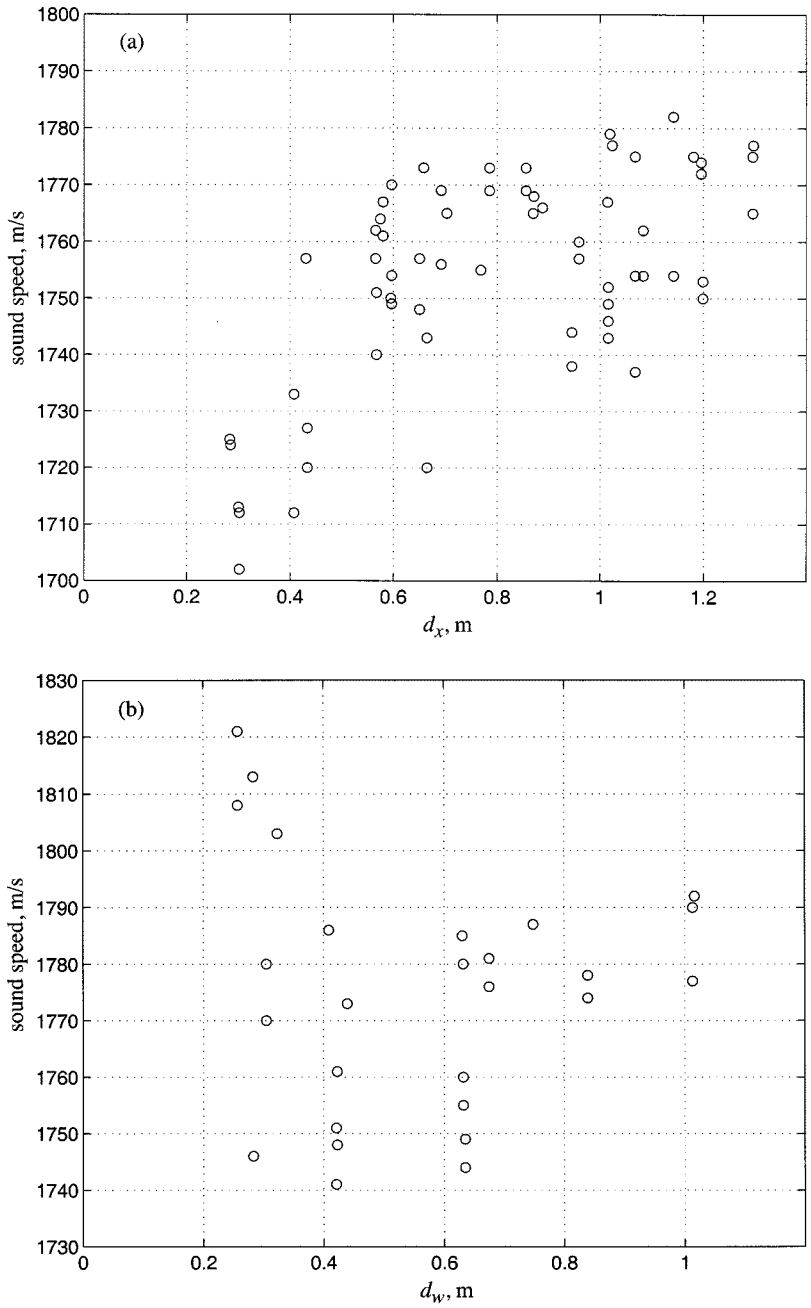

Fig. 15. Measured sound speed at stations 15 and 23 with probes 30-cm deep in the sediment, as a function of transducer separation. (a) Source-to-receiver path lengths, d_x, cross-correlation timing, and (29). Note the trend toward higher sound speeds at greater distances. (b) Receiver-to-receiver pathlengths, d_w, and inter-receiver correlation timing.

techniques proposed above. The mean sound speed was found to be 27 m/s faster than that returned by the source-to-receiver methods. Excluding the five measurements taken over differential path lengths of less than 20 cm, the values of the sound speed, although still quite variable (mean 1777 m/s, with spread between 1744 and 1821 m/s and a standard deviation of 21.3 m/s), exhibit no obvious systematic dependence on distance between the receivers [Fig. 15(b)].

Two sources of variability are present in the estimated sound speeds shown in Fig. 15(b): timing errors from the two source-to-receiver travel time measurements and variations from one deployment of the probes to next, which will be referred to as site-to-site variability. As discussed in Section V-D, the timing errors give rise to a variation in sound speed that scales inversely with separation and is approximately $\pm 0.25\%$ at a distance of 1 m, which equates to ± 4.5 m/s for a mean sound speed of 1777 m/s; and the site-to-site variability, estimated from separations greater than 1 m, is about ± 15 m/s. On combining these two effects, the total error in the estimated sound speeds in Fig. 15(b) is $E \approx \pm[(4.5(\mathrm{m}/d_w))^2 + (15)^2]^{1/2}$ m/s, which indicates that the spread in the data should be greater at shorter ranges. For $d_w = 0.3$ m, the total error is $E \approx \pm 21$ m/s compared with $E \approx \pm 15.7$ m/s when $d_w = 1$ m, which is consistent with the trend of the variations seen in Fig. 15(b). As a rule of thumb, it is recommended that the length of the inter-receiver travel path should be at least ten acoustic wavelengths, although even this

TABLE II
SUMMARY OF THE MEAN SOUND SPEEDS AND MEAN ATTENUATIONS AT 38 kHz AT THE SEVEN SAX99 STATIONS. THE NUMBERS IN BRACKETS ARE STANDARD DEVIATIONS. BELOW IS THE KEY TO THE TECHNIQUES USED TO ESTIMATE THE PARAMETERS. SR: SOURCE-TO-RECEIVER, CROSS-CORRELATION TIMING, (29). RR: RECEIVER-TO-RECEIVER AND AUTO-CORRELATION TIMING. T: TRANSPOSITION, (36). MS: MEAN-SQUARE, (35). TMS: MEAN-SQUARE + TRANSPOSITION

param. \ station (technique)	15 & 23	2	3	4	7	9	13
c_p(SR), m/s	1758(10.3)	1754(10.4)	---	---	1750(4.1)	1755(10.4)	---
c_p(RR), m/s	1777(21.3)	1772(12.6)	1779(9.2)	1785(16.6)	1768(7.2)	1781(6.4)	1779(8.8)
α_p(T), dB/m	---	10.6(2.5)	12.7(3.4)	9.1(6.6)	9.7(0.1)	13.4(3.4)	21.3(4.5)
α_p(MS), dB/m	13.3(7.8)	9.4(4.2)	13.6(4.2)	8.8(8.2)	9.8(5.1)	10.6(4.5)	21.7(5.6)
α_p(TMS), dB/m	---	10.6(2.5)	12.7(3.4)	9.1(6.6)	9.7(0.1)	13.4(3.4)	21.4(4.5)

may not be sufficient at lower frequencies where the signal-to-noise ratio is often low.

The sound speeds at the six primary stations, re-calculated using inter-receiver correlations, were not statistically different (t-test < 0.1) from those shown in Fig. 15(b) for stations 15 and 23. Table II shows a summary of the mean sound speeds at all stations, as estimated using source-to-receiver and receiver-to-receiver paths.

By averaging the inter-receiver data from all six primary stations, the mean sound speed was found to increase weakly with depth beneath the seawater-sediment interface: 1774 (12.8) m/s at 10 cm; 1778 (10.0) m/s at 20 cm; and 1781 (15.5) m/s at 30 cm, where the numbers in parentheses are standard deviations. By way of comparison, the measurements of the sound speed at 400 kHz (mean 1783 m/s, with spread between 1721 and 1788 m/s) made by Briggs [1] on diver-collected cores from the SAX99 site are only marginally higher than the values from ISSAMS at 38 kHz. This could indicate very weak frequency dispersion over the band between 38 and 400 kHz, of less than 0.5% per decade of frequency.

C. Attenuation Measurements

The attenuation at all eight ISSAMS stations in SAX99 was evaluated using three different techniques. The first relied on the ratio of the mean-square values of the pulse arrivals at two receivers, (35). Secondly, the attenuation was estimated using Richardson's transposition technique, (36); and finally, the attenuation was calculated using the transposition technique, (36), combined with mean-square values, (33) and (34). At all the sites, the mean values of the attenuation, as calculated by each of the three techniques, were not significantly different (Table II). For example, for the six primary stations, the attenuation from the mean square technique yielded a mean of 11.9 dB/m (range 2.2 to 29 dB/m and standard deviation 5.1 dB/m), compared with the transposition technique, which returned a mean of 11.7 dB/m (range 1.9 to 24.5 dB/m and standard deviation 5.3 dB/m). No appreciable systematic range dependence was observed in the attenuation estimates, as can be seen in Fig. 16, although at the shorter ranges, below 40 cm, there is a noticeably greater spread in the data. The origin of this enhanced spread is unclear but it can be stated that it does not arise from the amplitude resolution of the measurement system, which is of the order of 0.1%. Based on the trend exhibited by the data, it would seem prudent to make attenuation measurements over ranges that are at least ten wavelengths long.

In Table II, the standard deviation of the sound speed is of the order of 1%, whereas the standard deviation of the attenuation, even at the longer ranges, is close to 60%. Both percentages are typical of sandy sediments [21], and a significant component of both is site-to-site variability. The reason for such relative large excursions in the attenuation measurements cannot be stated with certainty but an important contributor, at least with the mean-square and spectral ratio techniques, could be poor coupling of the receivers to the granular sediment. If this were the case, the amplitudes of the pulse arrivals would be affected, giving rise to high site-to-site variability in the estimated attenuation, but the timing measurements yielding the sound speed would be relatively stable. Just to emphasize the point, the high variability of the attenuation is a site-to-site effect, suggesting that it may arise, at least partially, from the removal and re-insertion of the probes into the sediment. By comparison, the intrinsic measurement error in a single estimate of the attenuation, or in a sequence of estimates at different frequencies with the probes unmoved, is negligible.

XI. BROAD-BAND MEASUREMENTS OF SOUND SPEED AND ATTENUATION

During two deployments of ISSAMS, at stations 9 and 13, the frequency dependence of the sound speed and attenuation in the sediment was investigated by transmitting a sequence of 20 tone bursts with center frequencies ranging from 5 to 100 kHz in 5-kHz increments. All the input pulses were 6-cycles long and the receiver-to-receiver travel path was nominally 0.53 m. However, for two reasons, only the results for frequencies of 25 kHz and above are reported here: below 25 kHz, the source was inefficient with the result that the signal-to-noise ratio was too low to give reliable results; and at these lower frequencies, the acoustic path length was too short to satisfy the ten-wavelength criterion stated earlier.

For precision in estimating the wave speeds and attenuations, the inter-receiver distance was acoustically calibrated in seawater at each frequency. The transducers used for receiving and

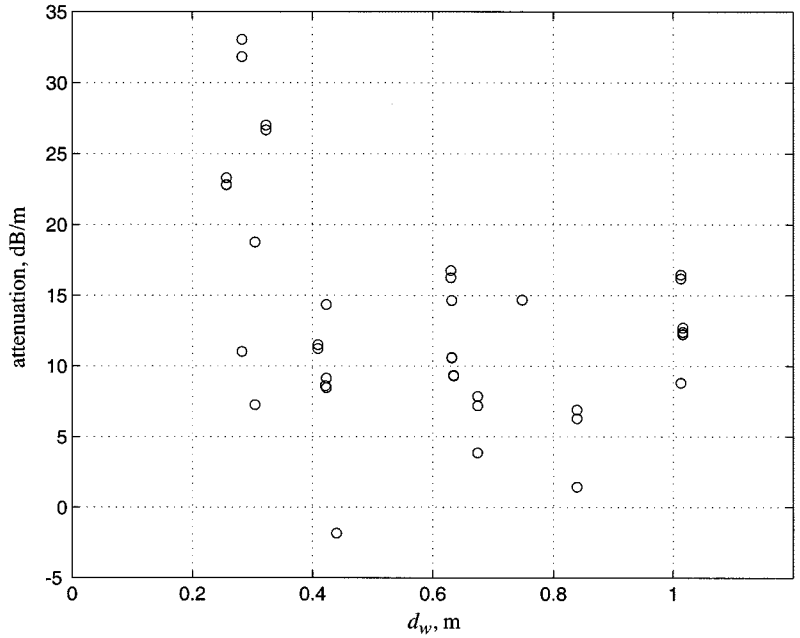

Fig. 16. Attenuation at 38 kHz estimated using the mean-square technique, (35), at stations 15 and 23, with probes 30 cm deep in the sediment, as a function of inter-receiver separation, d_w.

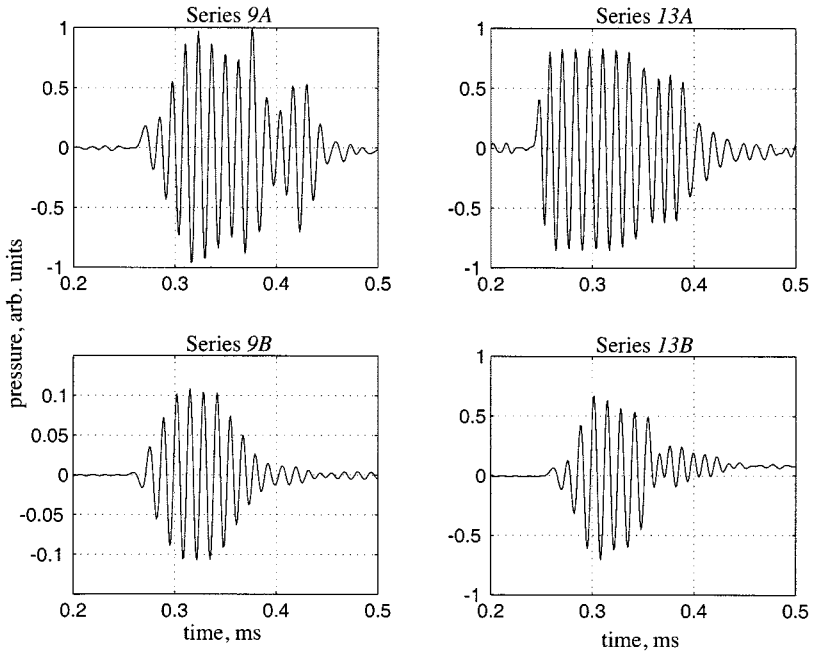

Fig. 17. Near-phone, 75 kHz arrivals in seawater. Note the extended duration of the two Series *A* signals relative to the more compact form of Series *B*.

transmitting were 1–3 piezoelectric composites with relatively broadband characteristics. It is important to note that the broadband measurements at stations 9 and 13 are expected to be much more stable than the data in Figs. 15 and 16 because the probes remained unmoved in the sediment during each sequence of transmissions and thus there is no site-to-site variability.

Receiver-to-receiver measurements were performed at the two stations using two nominally similar sources, designated A and B, one of which transmitted from left-to-right and the other from right-to-left across the receiver pair. The travel paths in the two opposing directions were close but not identical because the source–receiver–receiver–source configuration was not rectilinear, the transducers being offset to reduce the effects of shadowing and scattering. At both stations, each source was used to generate a set of inter-receiver, broadband sound-speed and attenuation data. The resultant four data sets are designated Series *9A* & *13A* and Series *9B* & *13B*.

Fig. 17 illustrates the 75 kHz pressure waveforms detected in seawater by the near-phone in the four Series. Note that both Series A arrivals are of extended duration relative to the more compact form of their Series B counterparts. The differences between the Series A and B waveforms are believed to be due

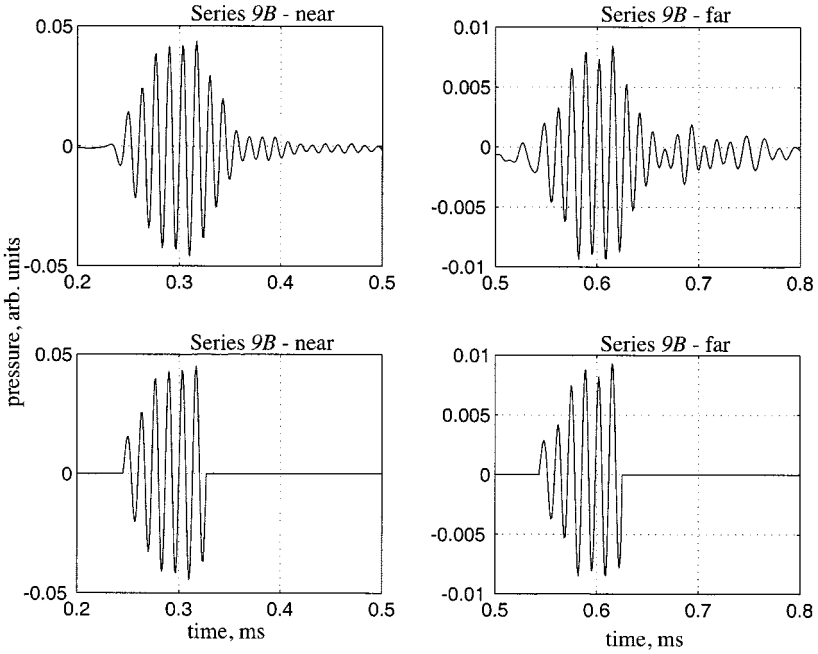

Fig. 18. Series *9B*, 75 kHz arrivals in sediment, raw data (a) near-phone and (b) far-phone. The same signals are shown in (c) and (d), respectively, after subtracting the mean level, windowing six cycles, and Butterworth filtering.

to an internal reflection from a backing plane within source A, although this remains to be confirmed. However, this interpretation is consistent with the following facts: the Series A waveforms generally contain significantly more cycles than the six that were transmitted; the number of additional cycles tends to rise as the frequency increases; and, as may be seen in Fig. 17, within the pulse arrivals there is evidence of phase shifting and amplitude modulation.

Unfortunately, the phase shifts will distort estimates of the wave speed because of the associated errors in timing; and the amplitude modulation will corrupt estimates of the attenuation. In view of these difficulties, the Series *9A* and *13A* data sets are excluded from the remaining discussion. By way of contrast, the Series *9B* and *13B* waveforms are of good quality, as exemplified in Fig. 17. In particular, they do not exhibit significant phase shifting or amplitude modulation. Accordingly, the Series *9B* and *13B* data sets form the basis of the following discussion on the broadband behavior of the sediment sound speed and attenuation.

A. Sound Speed and Attenuation Data

Typical sediment arrivals are illustrated in Fig. 18, which shows the 75 kHz, Series *9B* pressure time series, as detected at the near and far receivers. The raw data in panels (a) and (b) have been windowed and filtered in (c) and (d). As with all the arrivals, in seawater and sediment, the windowing was performed, after removing the mean level, by selecting several of the inner cycles of the pulse and zero-padding the leading and trailing regions. At every frequency, this zero-padding procedure was performed with great care on both water pulses and both sediment pulses. The two windowed signals in each pair were made exactly the same length, to avoid distorting the estimate of attenuation, and in each pair the same segment of signal was used, to minimize timing errors. Generally, the start of each windowed pulse coincided with the beginning of a positive half-cycle, as illustrated in panels (c) and (d) of Fig. 18. In addition, a low-pass Butterworth filter was applied to each windowed pulse to remove spurious high frequency components. The filtering had little effect on higher frequency pulses reported here, which have a high signal/noise ratio.

For each frequency, using the windowed pulses, the distance between the receivers was acoustically calibrated in seawater from the cross-correlation delay and also from the phase delay. Fourier and mean-square calibrations of the amplitude responses of the receivers were also performed in the water column. In the sediment, a good approximation to the group speed at each frequency was determined from the cross-correlation technique and the phase speed was found from phase-delay timing, (28). The attenuation was determined from the mean-square levels, (35), and also from the Fourier magnitudes, (32).

Fig. 19 shows the observed dispersion in the group speed and the phase speed from the Series *9B* and *13B* data sets, along with the associated broadband attenuations. In general, the attenuation estimates from the mean-square and Fourier techniques follow each other closely, and the same is true of the group speed and the phase speed. Note that at any given frequency, the attenuation at station 9 is significantly less than that at station 13, even though the sandy sediment at the two stations is nominally the same. At both stations, the attenuation shows a near-linear dependence on frequency, but the gradient of the two data sets differs by a factor of approximately 2. When referenced to 1 kHz, the attenuation is approximately 0.3 and 0.6 dB/m/kHz from Series *9B* and *13B*, respectively. This difference between the attenuation at the two stations may be indicative of a coupling effect. For reference, the numerical values of the wave speed and attenuation data in Fig. 19 are listed in Table I.

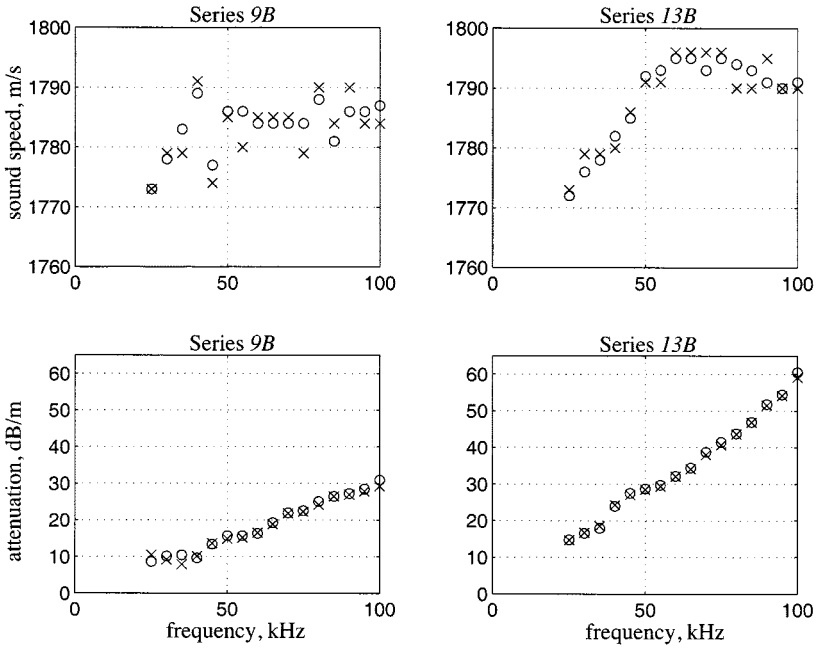

Fig. 19. Group speed from cross-correlation (crosses, ×) and phase speed from phase delay (circles, ○) as a function of frequency. Also shown are the broadband attenuations from mean-square levels (crosses, ×) and spectral amplitudes (circles, ○).

The main source of error in the wave speed measurements in Fig. 19 is the timing resolution of 10^{-6} s, set by the sampling rate. As discussed earlier, this intrinsic measurement error gives rise to a variation in the sound speed estimates that scales inversely with separation. This error amounts to approximately ± 5 m/s when the receivers are separated by 1 m. Thus, with a separation $d_w = 0.53$ m, as was the case for the data in Fig. 19, the estimated error is approximately ± 9 m/s.

B. Comparison With Inter-Granular Shearing Theory

The nearly constant Q and weak dispersion seen in Fig. 19 are qualitatively consistent with the expression for the complex sound speed in a saturated granular medium in (26). For a quantitative comparison, this expression may be split into its real and imaginary parts, allowing the phase speed to be written as

$$\frac{1}{c_p} = \frac{1}{c_o} \operatorname{Re}\left\{\frac{1}{q}\right\} \tag{37}$$

and the attenuation as

$$\alpha_p = -\frac{\omega}{c_o} \operatorname{Im}\left\{\frac{1}{q}\right\} \tag{38}$$

where

$$q = \sqrt{1 + \eta(j\omega T)^n}. \tag{39}$$

[*N.B.*, The imaginary part of $1/q$ is negative making the attenuation coefficient in (38) positive.]

The phase speed in the limit of low frequency, c_o, is given by Wood's equation

$$c_o = \sqrt{\frac{\kappa_o}{\rho_o}} \tag{40}$$

where κ_o and ρ_o are, respectively, the bulk modulus and density of the sediment. These quantities are the following weighted means:

$$\frac{1}{\kappa_o} = N\frac{1}{\kappa_w} + (1-N)\frac{1}{\kappa_g} \tag{41}$$

and

$$\rho_o = N\rho_w + (1-N)\rho_g, \tag{42}$$

where the subscripts w and g denote quantities relating to water and sand grains, respectively, and N is the porosity of the medium. Under the conditions prevailing when the data in Fig. 19 were collected, the following values are appropriate: $N = 0.37$, $\rho_w = 1026$ kg/m^3, $\rho_g = 2650$ kg/m^3, $\kappa_w = 2.42 \times 10^9$ Pa, and $\kappa_g = 3.6 \times 10^{10}$ Pa, which give $c_o = 1687$ m/s.

The two remaining parameters in (38) and (39), n and η, represent physical processes occurring at grain contacts but at present, unlike c_o, they cannot be evaluated from theoretical arguments. By treating them as adjustable, these parameters may be selected to give a "best" fit of (37) and (38) for the phase speed and the attenuation to the respective data sets. This procedure yields the solid curves in Figs. 20 and 21 for the Series *9B* and *13B* wave speeds and attenuations. It can be seen that for both stations, from 25 to 100 kHz, the grain-shearing theory follows the weakly dispersive trend of the wave-speed data reasonably well and the theory accurately matches the near-linear frequency dependence of the attenuation data.

C. Comparison With Biot Theory

To compare the predictions of the Biot theory with the phase speed and attenuation data, (25) is split into its real and imagi-

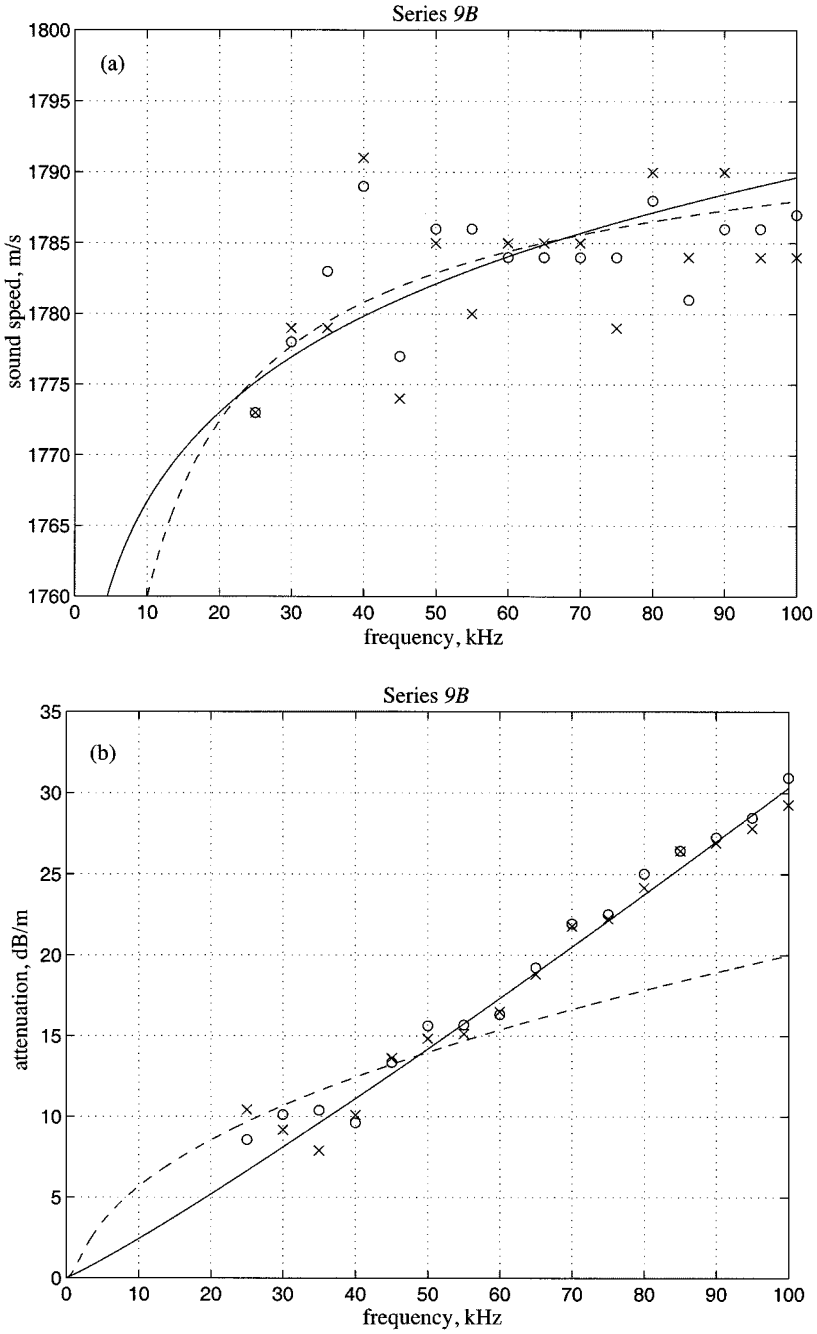

Fig. 20. (a) Wave speed; (b) attenuation as a function of frequency. The data (circles, ∘, and crosses, ×) are the same Series *9B* data points as in the top-left and bottom-left panels of Fig. 19. The solid lines are from the grain shearing theory, (37) and (38), with $c_o = 1687$ m/s, $n = 0.113$ and $\eta = 0.028$; and the broken lines are from the Biot theory, (43) and (44), with $c_o = 1687$ m/s, $c_\infty = 1800$ m/s and $\gamma = 0.08$ ms.

nary parts. The expression for the phase speed is then found to be

$$\frac{1}{c_p} = \left(\frac{1}{c_o} - \frac{1}{c_\infty}\right) \mathrm{Re}\left[\frac{1 - j\omega\gamma}{1 + \omega^2\gamma^2}\right]^{1/2} + \frac{1}{c_\infty} \qquad (43)$$

and the attenuation is

$$\alpha_p = -\omega\left(\frac{1}{c_o} - \frac{1}{c_\infty}\right) \mathrm{Im}\left[\frac{1 - j\omega\gamma}{1 + \omega^2\gamma^2}\right]^{1/2}. \qquad (44)$$

[*N.B.*, The imaginary part of the radical is negative making the attenuation coefficient in (44) positive.]

Since c_o in these expressions is given by Wood's equation, as in the grain-shearing theory, it takes the value $c_o = 1687$ m/s derived above, as appropriate to the condition of the SAX99 sediment at the time the Series *9B* and *13B* data were taken. From a visual inspection of the dispersion data, the values of the remaining two parameters in (43) and (44) are obtained for each of the data sets. This procedure yields the dashed curves in Figs. 20 and 21.

Like the data, the Biot wave speed shows weak dispersion in the frequency range between 25 and 100 kHz. The Biot attenuation, however, can be seen to exhibit the characteristics typical

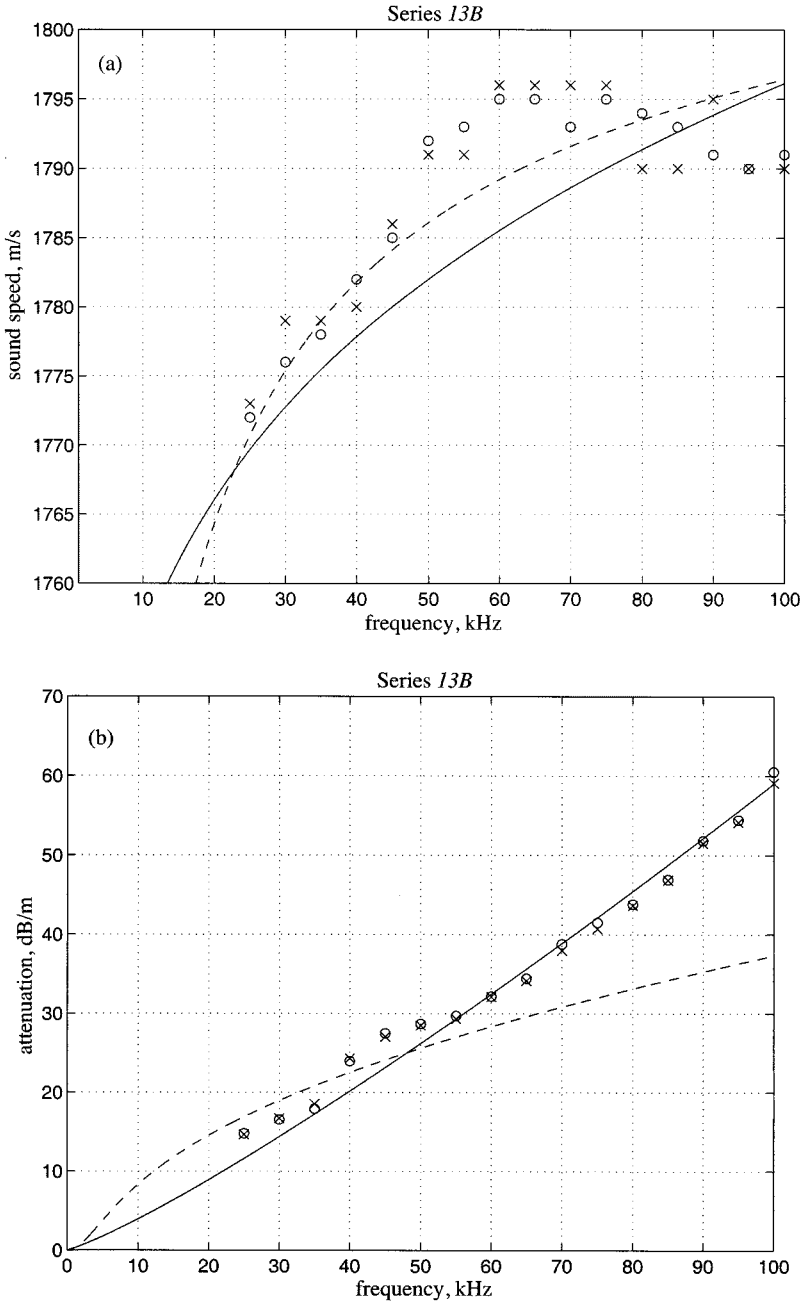

Fig. 21. (a) Wave speed; (b) attenuation as a function of frequency. The data (circles, ∘, and crosses, ×) are the same Series *13B* data points as in the top-right and bottom-right panels of Fig. 19. The solid lines are from the grain shearing theory, (37) and (38), with $c_o = 1687$ m/s, $n = 0.205$ and $\eta = 0.009$; and the broken lines are from the Biot theory, (43) and (44), with $c_o = 1687$ m/s, $c_\infty = 1820$ m/s and $\gamma = 0.03$ ms.

of viscous dissipation, that is, a low-frequency regime varying as the square of frequency, and a square-root dependence on frequency when $\omega\gamma > 1$. Such functional behavior can be seen to deviate significantly from the near-linear dependence on frequency exhibited by the Series *9B* and *13B* attenuation data sets.

XII. Concluding Remarks

Some of the subtleties of travel-time measurements using tone-bursts in a dispersive medium are discussed in this article. Such signals are usually transmitted by a narrow-band source transducer, which generally introduces significant amplitude and phase distortion into the output pulse. Moreover, the source "rings," thereby extending the duration of the output by several cycles. The pressure pulse transmitted into the medium is not, therefore, a facsimile of the input voltage. In fact, there is not even a one-to-one correspondence between the main features, for example, the principal maxima, of the input and output pulses. In general, the situation is exacerbated as the pressure pulse propagates away from the source because of dispersion and attenuation in the medium. Both phenomena introduce further distortion by continually modifying the spectral components in the pulse, an effect which is cumulative and therefore of more concern at longer ranges.

The distortion due to the source and to a lesser extent the medium has serious implications for high-precision travel-time

measurements in sediments. If some feature of the input, say one of the principal peaks, were used as a timing reference, the first problem would be to identify the corresponding feature in the pulse arrival at a receiver down range from the source. In fact, there is no corresponding feature, so if one were artificially selected, it would lead to a timing error. Similarly, if a correlation were performed between the input to the source and the arrival at the receiver, the correlation delay would not correspond to the travel time.

These timing difficulties can be overcome in many situations by ignoring the input pulse altogether and performing a travel-time measurement between the arrivals at two receivers, with one at approximately twice the range of the other. The two arrivals are equally distorted by the source and, although dispersion and attenuation are still present, their effects are often negligible on narrow-band pulses over practicable receiver-to-receiver ranges. Assuming this to be the case, a correlation applied to the two pulse arrivals will yield the travel time accurately at the center frequency of the transmission. If dispersion across the bandwidth of the pulse were not negligible, this inter-receiver correlation technique would be less satisfactory. Then, a Fourier decomposition of the two arrivals may be employed to yield the phase delay over the travel path, which, after phase unwrapping, provides the receiver-to-receiver travel time as a function of frequency. The Fourier technique may have useful application for broader band pulses, or over longer ranges in strongly dispersive media.

The receiver-to-receiver correlation technique and the Fourier decomposition are illustrated with tone-burst data from ISSAMS. ISSAMS was deployed during SAX99, an experiment performed in 1999 in the Gulf of Mexico to determine the properties of the well-sorted medium-sand marine sediment off Fort Walton Beach. From one particular deployment of ISSAMS, at a frequency of 38 kHz, the sound speed in the medium is found to be 1777 m/s from the auto- correlation analysis and 1779 m/s from the Fourier decomposition. The difference between these results is well within the resolution ($\pm$5 m/s) of the experimental data. For the same deployment, the attenuation, from two different methods, is found to be 17 dB/m at 38 kHz, which is comparable with the measurements of attenuation in marine sands of earlier investigators.

ISSAMS was deployed at seven stations around the SAX99 site. Using source-to-receiver ranges, the sound speeds calculated from the data are higher for the longer path lengths. Inter-receiver paths return sound speeds with no systematic range dependence. The values of attenuation estimated from the data show no obvious dependence on range, irrespective of whether source-to-receiver or inter-receiver paths are used. A statistical analysis of the data returned by ISSAMS from the SAX99 deployments yields a mean (inter-receiver) sound speed of 1777 m/s and a mean attenuation of 13.3 dB/m, with standard deviations, respectively, of the order of 1% and 60%. The relatively high site-to-site variability in the attenuation measurements, indicated by the latter figure, may be due to variable coupling of the receivers to the sediment at different locations.

Broadband measurements between 25 and 100 kHz are reported which yield the compressional wave speed and attenuation as functions of frequency. Over this band, the frequency dispersion is weak, and may be reasonably fitted by theoretical predictions from Biot's viscous-flow treatment of wave propagation in granular materials and also from Buckingham's wave-theoretical analysis based on grain-to-grain shearing. The attenuation exhibits a near-linear dependence on frequency over the experimental bandwidth, indicating an essentially constant Q. Such a property is consistent with the attenuation predicted from the grain-to-grain shearing theory, but not with the viscous dissipation of the Biot theory.

APPENDIX
SYSTEM FUNCTION OF THE SOURCE TRANSDUCER

Referring to the equivalent circuit for the acoustic source in Fig. 1, the output current, $i_2(t)$, is related to the transformer input current, $i_1(t)$, as follows:

$$I_2(j\omega) = -\frac{j\omega M I_1(j\omega)}{Z} \tag{A1}$$

where $I_{1,2}$ are the Fourier transforms of the two currents and the output impedance Z is

$$Z = \left[j\omega(L + L_2) + \frac{1}{j\omega C} + R \right]. \tag{A2}$$

The input voltage is given by

$$V = j\omega L_1 I_1 + j\omega M I_2 = \left[j\omega L_1 + \frac{\omega^2 M^2}{Z} \right] I_1. \tag{A3}$$

Since the mutual impedance of an ideal transformer is

$$M = \sqrt{L_1 L_2} \tag{A4}$$

the system function of the source, that is, the ratio of the voltage across the output resistance, $R = R_m + R_x$, to the voltage at the input, is easily shown to be

$$H(j\omega) \equiv \frac{I_2 R}{V} = \frac{H_o}{1 + jQ\left(\frac{\omega}{\omega_o} - \frac{\omega_o}{\omega}\right)} \tag{A5}$$

where ω_o and Q are the resonance parameters of the output circuit, as defined in (3) and (4), and

$$H_o = -\sqrt{\frac{L_2}{L_1}} \tag{A6}$$

is the gain of the circuit. The expression for the source system function in (A5) is used in the text.

ACKNOWLEDGMENT

The authors would like to thank several anonymous reviewers for their detailed and perceptive comments.

REFERENCES

[1] M. D. Richardson, K. B. Briggs, D. L. Bibee, P. A. Jumars, W. B. Sawyer, D. B. Albert, T. B. Berger, M. J. Buckingham, N. P. Chotiros, P. H. Dahl, N. T. Dewitt, P. Fleischer, R. Flood, C. F. Greenlaw, D. V. Holliday, M. H. Hulbert, M. P. Hutnak, P. D. Jackson, J. S. Jaffe, H. P. Johnson, D. L. Lavoie, A. P. Lyons, C. S. Martens, D. E. McGehee, K. D. Moore, T. H. Orsi, J. N. Piper, R. I. Ray, A. H. Reed, R. F. L. Self, J. L. Schmidt, S. G. Schock, F. Simonet, R. D. Stoll, D. J. Tang, D. E. Thistle, E. I. Thorsos, D. J. Walter, and R. A. Wheatcroft, "Overview of SAX99: Environmental considerations," *IEEE J. Ocean. Eng.*, vol. 26, pp. 26–53, Jan. 2001.

[2] E. I. Thorsos, K. L. Williams, N. P. Chotiros, J. T. Christoff, K. W. Commander, C. F. Greenlaw, D. V. Holliday, D. R. Jackson, J. L. Lopes, D. E. McGehee, J. E. Piper, M. D. Richardson, and D. Tang, "An overview of SAX99: Acoustic measurements," *IEEE J. Ocean. Eng.*, vol. 26, pp. 4–25, Jan. 2001.
[3] A. H. Reed, K. B. Briggs, and D. L. Lavoie, "Porometric properties of siliciclastic marine sand: A comparison of traditional laboratory measurements with image analysis and effective medium modeling," *IEEE J. Ocean. Eng.*, vol. 27, pp. 581–592, July 2002.
[4] D. Tang, K. B. Briggs, K. L. Williams, D. R. Jackson, and E. I. Thorsos, "Fine-scale volume heterogeneity measurements in sand," *IEEE J. Ocean. Eng.*, vol. 27, pp. 505–514, July 2002.
[5] R. A. Wheatcroft, "*In situ* measurements of near-surface porosity in shallow-marine sands," *IEEE J. Ocean. Eng.*, vol. 27, pp. 561–570, July 2002.
[6] M. J. Buckingham, "Theory of compressional and shear waves in fluid-like marine sediments," *J. Acoust. Soc. Amer.*, vol. 103, no. 1, pp. 288–299, 1998.
[7] O. K. Rice, "On the statistical mechanics of liquids, and the gas of hard elastic spheres," *J. Chem. Phys.*, vol. 12, no. 1, pp. 1–18, 1944.
[8] A. Barbagelata, M. Richardson, B. Miaschi, E. Muzi, P. Guerrini, L. Troiano, and T. Akal, "ISSAMS: An *in situ* sediment acoustic measurement system," in *Shear Waves in Marine Sediments*, J. M. Hovem, M. D. Richardson, and R. D. Stoll, Eds. Dordrecht, The Netherlands: Kluwer, 1991, pp. 305–312.
[9] S. R. Griffin, F. B. Grosz, and M. D. Richardson, "*In situ* sediment geoacoustic measurement system," *Sea Tech.*, vol. 37, no. 4, pp. 19–22, 1996.
[10] M. D. Richardson, "Attenuation of shear waves in near-surface sediments," in *High Frequency Acoustics in Shallow Water*, N. G. Pace, E. Pouliquen, O. Bergem, and A. L. Lyons, Eds. La Spezia, Italy: NATO SACLANT Undersea Research Centre, 1997, pp. 451–458.
[11] E. L. Hamilton, "Compressional-wave attenuation in marine sediments," *Geophys.*, vol. 37, no. 4, pp. 620–646, 1972.
[12] ——, "Acoustic properties of sediments," in *Acoustics and the Ocean Bottom*, A. Lara-Saenz, C. R. Cuierra, and C. Carbo-Fité, Eds. Madrid, Spain: Consejo Superior de Investigacions Cientificas, 1987, pp. 3–58.
[13] M. D. Richardson, "*In-situ*, shallow-water sediment geoacoustic properties," in *Shallow-Water Acoustics*, R. Zhang and J. Zhou, Eds. Beijing, China: China Ocean Press, 1997, pp. 163–170.
[14] W. S. Burdic, *Underwater Acoustic System Analysis*, 2nd ed. Englewood Cliffs, NJ: Prentice-Hall, 1991.
[15] M. A. Biot, "Theory of propagation of elastic waves in a fluid-saturated porous solid: I. Low-frequency range," *J. Acoust. Soc. Amer.*, vol. 28, no. 2, pp. 168–178, 1956.
[16] ——, "Theory of propagation of elastic waves in a fluid-saturated porous solid: II. Higher frequency range," *J. Acoust. Soc. Amer.*, vol. 28, no. 2, pp. 179–191, 1956.
[17] R. D. Stoll, *Sediment Acoustics*, S. Bhattacharji, G. M. Friedman, H. J. Neugebaur, and A. Seilacher, Eds. Berlin, Germany: Springer-Verlag, 1989, vol. 26, Lecture Notes in Earth Sciences.
[18] K. L. Williams, "An effective density fluid model for acoustic propagation in sediments derived from Biot theory," *J. Acoust. Soc. Amer.*, vol. 110, no. 5, pp. 2276–2281, 2001.
[19] K. L. Williams, D. R. Jackson, E. I. Thorsos, and D. Tang, "Comparison of sound speed and attenuation measured in a sandy sediment to predictions based on the Biot theory of porous media," *IEEE J. Ocean. Eng.*, vol. 27, pp. 413–428, July 2002.
[20] M. J. Buckingham, "Wave propagation, stress relaxation, and grain-to-grain shearing in saturated, unconsolidated marine sediments," *J. Acoust. Soc. Amer.*, vol. 108, no. 6, pp. 2796–2815, 2000.
[21] M. D. Richardson and K. B. Briggs, "On the use of acoustic impedance values to determine sediment properties," in *Acoustic Classification and Mapping of the Seabed*, N. G. Pace and D. N. Langhorne, Eds. Bath, U.K.: University of Bath, 1993, vol. 15, pp. 15–24.

Michael J. Buckingham received the B.Sc. (*honors*) degree in physics and the Ph.D. degree in solid-state physics, both from the University of Reading, Reading, U.K in 1967, and 1971, respectively.

After a three year, entirely unsuccessful, post-doctoral effort to detect gravitational radiation from energetic stellar events, for which he received the Clerk Maxwell Premium from the I.E.R.E. (U.K.) in 1972, he abandoned cosmology in favor of underwater acoustics research at the Royal Aerospace Establishment, Farnborough, U.K., where he became an Individual Merit Senior Principal Scientific Officer, which allowed him the freedom to pursue his own research interests. He was an Exchange Scientist at the Naval Research Laboratory, Washington, DC and a visiting professor in the Department of Ocean Engineering, Massachusetts Institute of Technology, Cambridge. From 1988 to 1992, he was the U.K. National Representative on the Scientific Committee of the Marine Science and Technology (MAST) Program, Commission of European Communities, Brussels, Belgium. He is currently a Professor of ocean acoustics in the Marine Physical Laboratory, Scripps Institution of Oceanography, University of California, San Diego. He is an Editor-in-Chief of the *Journal of Computational Acoustics* and Editor of *Reviews in Physical Acoustics for the Journal of Sound and Vibration*, Academic Press. Concurrently with his position at Scripps, he is a Visiting Professor at the Institute of Sound and Vibration Research, University of Southampton, U.K. His research has been reported in over 200 papers in the scientific literature and he has also published a book on *Noise in Electronic Devices and Systems*.

Prof. Buckingham is a founder member of the Acoustical Oceanography Technical Committee of the Acoustical Society of America. He is a Fellow of the Acoustical Society of America, the Institute of Acoustics (U.K.), the Institute of Electrical Engineers and a Chartered Engineer (U.K.), and the Explorers Club. He is a member of the New York Academy of Sciences and of Sigma Xi. In 1982, he was the recipient of the A. B. Wood Medal from the Institute of Acoustics and has since received a number of other awards for his research.

Michael D. Richardson received the B.S. degree in oceanography from the University of Washington, Seattle, in 1967, the M.S. degree in marine science from the College of Williams and Mary, Williamsburg, VA, in 1971, and the Ph.D. degree in oceanography from Oregon State University, Corvallis, in 1976.

He began working at the Naval Ocean Research and Development Activity, now part of the Naval Research Laboratory (NRL), Stennis Space Center, MS, in 1977. Except for a five-year assignment as Principle Scientist at NATO's SACLANTCEN, La Spezia, Italy (1985–1989), he has worked at NRL as a Research Scientist and is currently head of the Seafloor Sciences Branch in the Marine Geosciences Division. His research interests include the effects of biological and physical processes on sediment structure, behavior, and physical properties near the sediment-water interface in both shallow-water coastal regions and in the deep sea. His current research is linked to high-frequency acoustic scattering from and propagation within the seafloor and prediction of mine burial.

Dr. Richardson is a member of the Acoustical Society of America, the American Geophysical Union, the European Geophysical Society, and Sigma Xi.